Preprint typeset using LaTeX style emulateapj v. 04/03/99

arXiv:astro-ph/9807312v3 18 Oct 2000

A MEASUREMENT OF ANISOTROPY IN THE COSMIC MICROWAVE BACKGROUND ON 7′-22′ SCALES

E.M. Leitch[1], A.C.S. Readhead, T.J. Pearson
California Institute of Technology, 105-24
Pasadena CA 91125
S.T. Myers[2]
University of Pennsylvania
209 S. 33rd St./Philadelphia PA 19104.
S. Gulkis, C.R. Lawrence
Jet Propulsion Laboratory, California Institute of Technology
4800 Oak Grove Dr./Pasadena CA 91109

ABSTRACT

We report a measurement of anisotropy in the cosmic microwave background radiation (CMBR) on $7' - 22'$ scales. Observations of 36 fields near the North Celestial Pole (NCP) were made at 31.7 and 14.5 GHz, using the 5.5-meter and 40-meter telescopes at the Owens Valley Radio Observatory (OVRO) from 1993 to 1996. Multi-epoch VLA observations at 8.5 and 15 GHz allow removal of discrete source contamination. After point-source subtraction, we detect significant structure, which we identify with emission from a combination of a steep-spectrum foreground and the CMBR. The foreground component is found to correlate with *IRAS* 100 μm dust emission. Lack of Hα emission near the NCP suggests that this foreground is either high-temperature thermal bremsstrahlung ($T_e \gtrsim 10^6$ K), flat-spectrum synchrotron or an exotic component of dust emission. On the basis of low-frequency maps of the NCP, we can restrict the spectral index of the foreground to $\beta \geq -2.2$. Although the foreground signal dominates at 14.5 GHz, the extracted CMBR component contributes 88% of the variance at 31.7 GHz, yielding an rms fluctuation amplitude of $82^{+12.1}_{-9.1}$ μK, including 4.3% calibration uncertainty and 12% sample variance (68% confidence). In terms of the angular power spectrum, $C_l = \langle |a_l^m|^2 \rangle$, averaged over a range of multipoles $l = 361 - 756$, the detected broadband amplitude is $\delta T_{l_e} \equiv [l(l+1)C_l/2\pi]^{1/2} = 59^{+8.6}_{-6.5}$ μK. This measurement, when combined with small angular-scale upper limits obtained at the OVRO, indicates that the CMBR angular power spectrum decreases between $l \sim 600$ and $l \sim 2000$ and is consistent with flat cosmological models.

Subject headings: cosmic microwave background — cosmology: observations

1. INTRODUCTION

In standard cosmological scenarios, baryonic matter decouples from the radiation field at $z_{dec} \simeq 1100$. Thus, the horizon scale at decoupling separates scales of importance for structure formation from scales which probe only the primordial spectrum of perturbations. For $z \gg 1$, the Hubble radius subtends an angle $\Delta\theta_H \approx 0°.87\,\Omega_0^{1/2}(z/1100)^{-1/2}$, so that for $\Omega_0 = 1$, angles $\gtrsim 1°$ correspond to physical scales which were outside the horizon at decoupling (see, e.g., Kolb & Turner 1990). On scales $\lesssim 1°$, anisotropies are directly linked to causal physical processes in the early universe. Specifically, they record the amplitude and phase of acoustic oscillations in the baryon-photon plasma and as such provide a direct measure of the cosmological parameters which govern the early universe.

In this paper, we present results from an experiment designed to detect CMBR anisotropy on $7' - 22'$ scales ($l \simeq 600$). This "RING5M" experiment is the most recent in a series of filled-aperture, ground-based anisotropy experiments at the Owens Valley Radio Observatory (OVRO). Previous experiments at the OVRO include the NCP experiment (Readhead et al. 1989), in which the OVRO 40-meter telescope was used to place a 95% confidence upper limit of $\Delta T/T < 1.7 \times 10^{-5}$ on power at $2'$ scales, and the RING40M experiment (Myers et al. 1993), which resulted in a detection of anisotropy, attributed to foreground contamination, of $2.3 \times 10^{-5} < \Delta T/T < 4.5 \times 10^{-5}$ (95% confidence) at the same resolution.

Since the *COBE* detection of a CMBR quadrupole in 1992 (Smoot et al. 1992), a large number of experiments have reported detections of anisotropy on $\gtrsim 1°$ scales (see Hancock et al. 1998, Bond 1996 for recent reviews). The RING5M is one of the few experiments to probe the region of l-space between these experiments and the high-l range of the earlier OVRO work (recent results from the CAT telescope (Scott et al. 1996) provide the only other detection on comparable scales).

Section §2 of this paper provides an overview of the RING5M experiment, while §3 and §4 review the data acquisition and relevant receiver characteristics in greater detail. Sections §5 and §6 describe the calibration of both telescopes used in the RING5M experiment; data selection and editing are described in §7. Results are presented in §7-§9, in which we also explore the data for internal consistency and describe tests for possible sources of systematic error. The results of an 8.5 GHz VLA survey of

[1]Present address: University of Chicago, 5640 S. Ellis Ave., Chicago IL 60637.

[2]Present address: National Radio Astronomy Observatory, P.O. Box 0, Socorro, NM 87801

the RING5M fields and subsequent multi-frequency monitoring of point sources for subtraction from the anisotropy data are presented in §10, while contamination by Galactic foregrounds is discussed in §11. Sections §12-§15 describe the detected CMBR anisotropy. The paper concludes with a discussion of the significance of our result for cosmological models.

2. THE EXPERIMENT

Observations were conducted at the OVRO from 1993 to 1996, using HEMT-amplified radiometers on the OVRO 5.5-meter and 40-meter telescopes, fully-steerable parabolic reflectors with Cassegrain focus (5.5-meter) and primary focus (40-meter). At 31.7 GHz, the resolution of the 5.5-meter telescope is $7'.37$ (FWHM). At 14.5 GHz, the OVRO 40-meter telescope provides a second frequency channel, for spectral discrimination of foregrounds. Since full illumination of the 40-meter telescope at 14.5 GHz would produce a $\sim 2'$ beam, the feeds were designed to illuminate an ~ 11 m patch on the dish surface, providing a good match to the the 5.5-meter beam at 31.7 GHz (see Table 1). The 14.5 GHz receiver is mounted in an off-axis configuration to minimize shadowing by the prime focus cage as well as scattering from the prime focus support legs, thereby reducing the effect of ground spillover. This makes the beamwidth a strong function of focus position and hence of zenith angle; the beam can vary by as much as an arcminute over the full zenith angle range. As a result, all observations at 14.5 GHz were restricted to lie within $\pm 5^\circ$ of the observing zenith angle for the Ring, $Z_{\rm Ring} \simeq 50^\circ$ (see below).

The 5.5-meter telescope is illuminated from the Cassegrain focus, so that the largest sidelobes of the feed illumination pattern see the sky instead of the ground, and the total contribution of the ground to the system temperature at 31.7 GHz is 6 K. Although the 14.5 GHz receiver is located at the prime focus of the 40-meter telescope, the under-illumination of the 40-meter dish results in a primary antenna pattern having its first sidelobes directed at the sky, and the ground contributes < 1 K to the system temperature.

On both telescopes, the receiver input is continuously switched at 500 Hz between two feed horns separated by $\sim 22'$ on the sky; the recorded signal is the difference between successive millisecond integrations from alternate feeds. On the 5.5-meter telescope, the columns of air seen by the two feeds overlap in area by $> 10\%$ to 400 m, while on the 40-meter, the columns overlap by $> 10\%$ to 1 km, and the fast ("Dicke") switching freezes out atmospheric fluctuations which occur in both beams simultaneously, at the same time suppressing $1/f$ noise from receiver components. During each measurement, azimuthal nodding of the telescopes between two symmetric positions, offset by the $22'$ beamthrow, provides an additional level of spatial switching, removing constant offsets or linear temperature gradients from the sky or ground (see §3). This "double switching" technique has been used successfully in both previous OVRO anisotropy experiments.

In the RING5M experiment, we observe 36 fields spaced by the $22'$ beamthrow in a ring around the North Celestial Pole (NCP). Field positions are given in Table 2. In order to suppress variations in the observed differential ground temperature introduced by telescope motion, fields are observed only within $\pm 5^\circ$ ($\pm 20^m$) of upper culmination (transit, at $Z_{\rm Ring} \simeq 50^\circ$). Near transit, the separation of neighboring RING5M fields is approximately azimuthal, so that if we denote the temperature in each field by T_i, the quantity which results from the double switching is given by

$$\Delta T_i = T_i - \frac{1}{2}(T_{i-1} + T_{i+1}). \quad (1)$$

The effective beam pattern produced by the switching is shown in Figure 1.

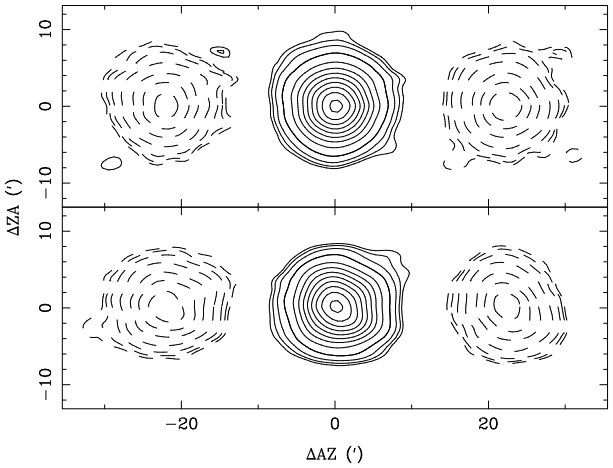

FIG. 1.— Measured double-switched beam pattern at 31.7 GHz (top panel) and 14.5 GHz (bottom), obtained by scanning across point sources. Contours are -0.5 to -0.1 in steps of 0.1, -0.05, -0.03, -0.02, 0.02, 0.03, 0.05 and 0.1 to 1.0 in steps of 0.1. For observations of the Ring, the symmetric negative beams correspond to the adjacent RING5M fields.

The interlocked geometry of the RING5M fields not only serves to eliminate systematic differences between observations of different fields, but also provides a boundary condition $\sum_i \Delta T_i = 0$ which can be checked for residual systematics. Moreover, point sources in a RING5M field can be identified by the characteristic minus-plus-minus signature they produce in successive fields.

3. OBSERVATIONS

In all of the observations presented here, the telescope alternates the beams (referred to as the ANT and REF beams) on source by slewing in azimuth by an amount $\pm\Delta\phi$ equal to the separation of the feed horns. The telescope integrates for equal times τ_s in each of four successive configurations, referred to as the A, B, C and D fluxes, shown schematically in Figure 2. In combination with the fast differencing between the feeds (ANT$-$REF), this procedure, known as a "FLUX" procedure, forms the basic double switching used to eliminate power gradients from the atmosphere or ground (see also Readhead et al. 1989, Myers et al. 1997). The $\pm\Delta\phi$ positions are referred to as *reference fields*.

To reduce systematic effects associated with varying slew times and settling of the telescope structure (particularly on the 40-meter telescope), an adjustable idle time τ_i is inserted between the A and B integrations and between the C and D integrations. Because the telescope does not move between the B and C integrations, no time delay is inserted there. The total duration of a FLUX procedure

TABLE 1
PARAMETERS FOR THE OVRO 5.5-M AND 40-M TELESCOPES

		5.5-meter	40-meter
Center Frequency (GHz)	ν_c	31.7	14.5
Bandwidth (GHz)	$\Delta\nu$	6	3
RMS Sensitivity (mK $s^{1/2}$)	$\sigma_{\rm rms}$	1.4	2.3
Major Axis Beamwidth (FWHM)	$\theta_{\rm maj}$	$7'.40 \pm 0'.26$[a]	$7'.80 \pm 0'.97$[a]
Minor Axis Beamwidth (FWHM)	$\theta_{\rm min}$	$7'.34 \pm 0'.25$[a]	$7'.17 \pm 0'.81$[a]
Beamthrow	$\Delta\phi$	$22'.16$	$21'.50$
Main Beam Solid Angle (10^{-6}sr)	Ω_m	5.21 ± 0.03	5.35 ± 0.02
Beam Solid Angle (10^{-6}sr)	Ω_a	7.92 ± 0.28	7.28 ± 0.28
Beam Efficiency	η_b	0.658 ± 0.024	0.735 ± 0.029
Aperture Efficiency	η_a	0.476 ± 0.017	... [b]
Sensitivity (mK Jy^{-1})	Γ	4.10 ± 0.15	21.30 ± 0.82

[a]Parameters are for the average of the ANT and REF beams.

[b]For the under-illuminated 40-meter telescope, the physical aperture is not well determined (see §6).

is thus $\tau = 4\tau_s + 2\tau_i$. For all of the RING5M observations presented here, $\tau_s = 20^s$ and $\tau_i = 10^s$, so that a FLUX procedure typically requires 100^s. For each set of measurements, the quantity

$$\mathrm{FLUX} = \frac{1}{2}(\Delta T_B + \Delta T_C - \Delta T_A - \Delta T_D) \qquad (2)$$

is formed, with associated standard deviation (SD) estimated by summing the variances of the individual (A-D) integrations.

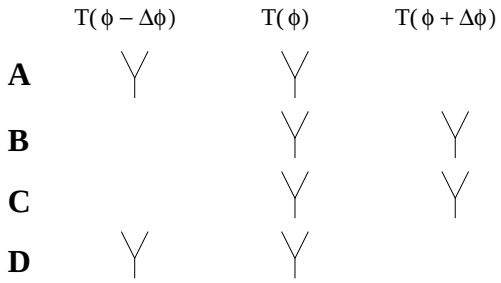

FIG. 2.— Double switching pattern in a FLUX procedure, shown here for an arbitrary temperature field on the sky. The sense of the beams is ANT left, REF right.

From Figure 2, it can be seen that the Dicke switching produces

$$\begin{aligned} \Delta T_{A,D} &= T(\phi - \Delta\phi) - T(\phi) \\ \Delta T_{B,C} &= T(\phi) - T(\phi + \Delta\phi), \end{aligned} \qquad (3)$$

so that the double-switched FLUX is given by

$$\begin{aligned} \mathrm{FLUX} &= \{T(\phi) - T(\phi + \Delta\phi)\} \\ &\quad - \{T(\phi - \Delta\phi) - T(\phi)\} \\ &\simeq -\Delta\phi^2 \left.\frac{\partial^2 T}{\partial \phi^2}\right|_\phi . \end{aligned} \qquad (4)$$

(In Eq. 1, T_{i+1} and T_{i-1} are the temperatures at the $\pm\Delta\phi$ positions, respectively.) If a source under observation is smaller than the beamthrow of the telescope, i.e., $T_{\rm src}(\phi + \Delta\phi) = T_{\rm src}(\phi - \Delta\phi) = 0$, from Eq. 4 we see that the contribution to the FLUX is just $2T_{\rm src}(\phi)$, or twice the power increment that would be measured with a single-difference observation.

On both telescopes, gain variations in the amplifiers are removed by referencing to noise diodes. Signals from the diodes are injected just behind the feed horns (see Figure 3) and are subject to the same receiver gain variations as the astronomical signal. The diode measurement, known as a "CAL" procedure, is identical to the FLUX procedure just described, with the exception that the telescope does not move between the A and B or the C and D integrations. The diode remains off during the A and D integrations and is turned on during the B and C integrations, so that from Eq. 2, the recorded CAL is just $T_{\rm diode}$.

4. RECEIVER CHARACTERISTICS

On the 5.5-meter telescope, load switches identical to the Dicke switch provide an observing mode where the background power is input from two internal loads of temperature $T_L \simeq 20$ K, providing a stable background against which to measure the noise diode powers even during periods of bad weather. On the 40-meter telescope, no internal loads are available, and all diode measurements are performed against the sky.

Both receivers exhibit a small degree of non-linearity, i.e., the measured power increment against a source in the presence of the typical background power level underestimates the power increment at the front of the feeds by $5 - 10\%$ (see Leitch 1998 for details). As a result, care must be exercised when comparing noise diode measurements against the internal loads to observations against the sky, as the background powers are in general different, leading to variations in the FLUX/CAL ratio as large as 6%. On both receivers, this effect has been measured and can be removed to high accuracy; at both frequencies, the non-linearity correction contributes $\lesssim 1\%$ to the final calibration error.

Table 2
Coordinates of the Ring5m Fields

Field	α(J2000)	δ(J2000)
OV5M0024	00:24:45.1	87:55:01
OV5M0104	01:05:25.9	87:54:55
OV5M0144	01:46:04.6	87:54:47
OV5M0224	02:26:40.0	87:54:36
OV5M0304	03:07:10.9	87:54:20
OV5M0344	03:47:36.5	87:54:03
OV5M0424	04:27:55.9	87:53:43
OV5M0504	05:08:08.6	87:53:20
OV5M0544	05:48:14.3	87:52:59
OV5M0624	06:28:12.9	87:52:37
OV5M0704	07:08:04.4	87:52:14
OV5M0744	07:47:49.2	87:51:53
OV5M0824	08:27:27.8	87:51:33
OV5M0904	09:07:00.9	87:51:16
OV5M0944	09:46:29.2	87:51:02
OV5M1024	10:25:53.8	87:50:51
OV5M1104	11:05:15.7	87:50:43
OV5M1144	11:44:35.9	87:50:41
OV5M1224	12:23:55.7	87:50:41
OV5M1304	13:03:16.2	87:50:45
OV5M1344	13:42:38.5	87:50:53
OV5M1424	14:22:03.8	87:51:06
OV5M1504	15:01:33.1	87:51:20
OV5M1544	15:41:07.2	87:51:37
OV5M1624	16:20:47.1	87:51:57
OV5M1704	17:00:33.3	87:52:18
OV5M1744	17:40:26.2	87:52:41
OV5M1824	18:20:26.2	87:53:03
OV5M1904	19:00:33.4	87:53:26
OV5M1944	19:40:47.6	87:53:47
OV5M2024	20:21:08.8	87:54:07
OV5M2104	21:01:35.1	87:54:24
OV5M2144	21:42:07.1	87:54:38
OV5M2224	22:22:43.2	87:54:49
OV5M2304	23:03:22.5	87:54:57
OV5M2344	23:44:03.1	87:54:53

TABLE 3
ABSOLUTE FLUX DENSITY AND TEMPERATURE SCALE

Source	31.7 GHz[a]	14.5 GHz[b]
Jupiter	$\mathbf{152 \pm 5}$ K	175 ± 9 K
DR 21	20.60 ± 0.68 Jy[c]	$\mathbf{22.87 \pm 1.07}$ Jy[c]
Cas A	164.18 ± 5.45 Jy[c]	313.04 ± 14.8 Jy[c]
Crab	307.15 ± 10.14 Jy[c]	426.9 ± 20.17 Jy[c]
3C 84	···	25.84 ± 1.26 Jy
3C123	···	5.85 ± 0.28 Jy
3C 218	···	4.69 ± 0.23 Jy
3C 286	2.02 ± 0.07 Jy	3.80 ± 0.22 Jy
3C 353	···	8.44 ± 0.40 Jy
NGC 7027	···	6.20 ± 0.30 Jy

[a]Assuming a brightness temperature for Jupiter of 152 ± 5 K at 31.7 GHz and $\Omega_{\rm Jup} = 6.656 \times 10^{-7}$ sr at 1 au.

[b]Assuming a ratio of $S_{\rm DR\ 21}(14.5\ {\rm GHz})/S_{\rm DR\ 21}(31.7\ {\rm GHz})$ given by Eq. 7.

[c]Flux density as seen by the telescope beam; not an accurate measure of absolute flux density.

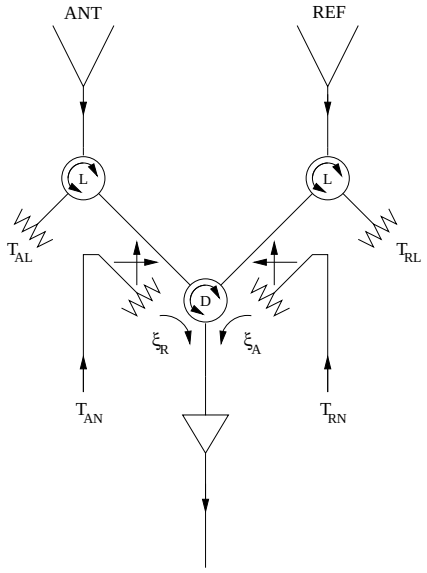

FIG. 3.— A schematic of the 31.7 GHz receiver front end. $T_{\rm AL}$ and $T_{\rm RL}$ represent the contribution to the system temperature of the ANT and REF internal loads, respectively. Similarly, $T_{\rm AN}$ is the temperature of the noise diode on the ANT side. The isolation of the Dicke switch (denoted D) when pointed at the ANT side is indicated by ξ_A and when pointed to the REF side, by ξ_R.

The fast switching is accomplished by a Dicke switch — a three-port, wide-band circulator whose direction is determined by the polarity of the magnetic field within its ferrite core. With the switch directed at one input port, a small amount of signal from the other input port is transmitted to the output port, typically at the level of $1-2\%$, known as the *isolation*, denoted ξ. The directional isolations of the switch, i.e., the isolations with the switch in ANT or REF position, denoted ξ_A and ξ_R respectively, depend sensitively on the impedance match at the three ports and in general are not equal.

From Figure 2, it can be seen that if $\xi_A \neq \xi_R$, even a linear temperature gradient can partially survive the double switching, contributing an additional term

$$\Delta{\rm FLUX} \simeq \Delta\phi \frac{\partial T}{\partial \phi}(\xi_{\rm R} - \xi_{\rm A}), \tag{5}$$

to Eq. 4, which, given typical values of ξ_A and ξ_R, can be as large as 100 μK for sky gradients as small as 1 mK/arcminute. We believe this effect to be responsible for year-to-year fluctuations in the mean observed in the RING5M data (see §7.4), which we expect a priori to be zero (see §2).

5. FLUX DENSITY SCALE

At 31.7 GHz, the flux density scale of the 5.5-meter telescope is based on a 31.4 GHz measurement of the brightness temperature of Jupiter,

$$T_J = 152 \pm 5\ {\rm K} \tag{6}$$

(Dent 1972). During 1996, daily calibration of the internal noise diodes at both frequencies was achieved by comparison with a set of secondary standards whose flux densities were measured relative to Jupiter (see Table 3), using an ephemeris distance for Jupiter and assuming $\Omega_{\rm Jup} = 6.656 \times 10^{-7}$ sr at 1 au. Ratios to Jupiter were determined at three epochs during which calibrator sources were observed for several days, as well as from daily observations of the sources (see below). Although the supernova remnants Cas A and the Crab nebula are partially resolved on both the 5.5-meter telescope and the under-illuminated 40-meter telescope ($\theta_{\rm snr} \sim 4'$), pointing on these sources has proven reproducible to high precision, making them suitable as relative calibrators.

Daily calibrator observations were interleaved with observations of the RING5M fields, so that every twelfth field (every eight hours) was replaced by a 40-minute scan on a calibrator source. To avoid selective depletion of data from any three fields, the set of secondary calibrators was chosen so that at least one would be visible at any time, and calibrator scans were precessed daily by one field, resulting in a uniform reduction in sensitivity of only 4% over

the entire Ring. At 14.5 GHz, observations of calibrator sources were restricted to lie within $\pm 5^\circ$ of the zenith angle of the Ring, and a correspondingly larger set of secondary calibrators was used to satisfy this condition.

5.1. *DR 21 and the 14.5 GHz Flux Density Scale*

The 31.4 GHz brightness temperature of Jupiter in Eq. 6 is based on a fit to the spectrum of the HII region DR 21,

$$S_\nu = 26.78 - 5.63 \log \nu_{\rm GHz} \text{ Jy}, \tag{7}$$

with an associated error of $\pm 3\%$ over the range $7-40$ GHz (Dent 1972). Because of its location in a complicated region of the Galactic plane, DR 21 itself is not used as an absolute calibrator in this experiment. Since the reference fields in a FLUX procedure are displaced azimuthally by $22'$ (see Figure 1), as DR 21 is tracked on the sky, emission in the ring of radius $22'$ around the source rotates through the reference beams, making the measured flux density a function of the source parallactic angle ψ_p, defined as the anglebetween the great circle passing through the source and the zenith and the great circle passing through the source and the celestial poles (throughout this paper, we have folded the parallactic angle into the range $(-90^\circ, 90^\circ)$) (see Figure 4). Independent scans on DR21, however, agree over the full parallactic angle range to within the scatter of the data. The resultant variation in the apparent flux density of DR 21 can therefore be removed, making it suitable as a relative calibrator.

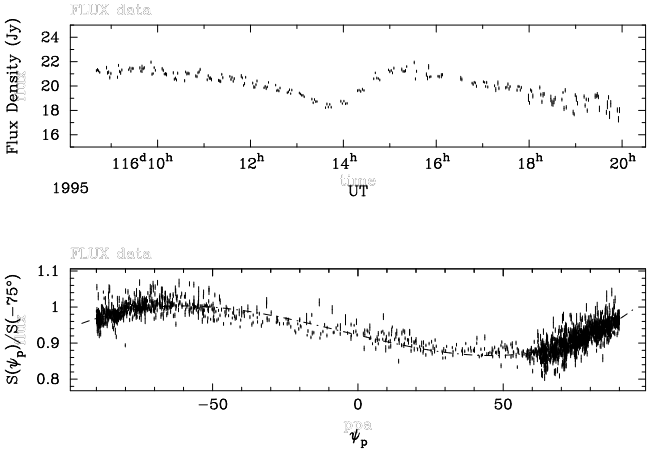

FIG. 4.— (Top panel) A typical scan on DR 21. The apparent flux density is dominated by contamination in the reference beams and is a strong function of parallactic angle. (Bottom) Dependence of the switched flux on parallactic angle, shown here in a compilation of 34 independent tracks on DR 21 from 1995. Each scan was separately calibrated and normalized to the flux over the ψ_p interval $(-80^\circ, -70^\circ)$. Shown also is the best fit model for the ψ_p dependence.

It is found that the fit to $S_{\rm DR\ 21}(\psi_p)$ derived at 31.7 GHz also removes the parallactic angle dependence of the flux density at 14.5 GHz, indicating that the contaminating flux in the reference fields has the same spectrum as DR 21 between 31.7 and 14.5 GHz. This is not surprising, since all of the emission in the region surrounding DR 21 is thought to belong to the same HII complex. Since the frequency dependence of the contaminating flux is separable from its parallactic angle dependence, the observed flux *ratio* at the two frequencies should follow from Eq. 7, and this fact can be used to establish a 14.5 GHz flux density scale relative to the same measurement of Jupiter at 31.4 GHz. The flux density scale so derived is in excellent agreement with the 14.5 GHz measurement of Jupiter's brightness temperature relative to DR 21 obtained by Gary (1974), using the Goldstone 64-m telescope. Therefore this scale, with the 5% errors reported by Gary, is the one used to calibrate the 14.5 GHz data.

5.2. *Cas A and Re-calibration of the Saskatoon Experiment*

The Saskatoon group has recently reported a measurement of intrinsic anisotropy relative to a fit to the spectrum of Cas A (Netterfield et al. 1997). The power they detect on degree scales has led to speculation that their assumed flux density for Cas A may be too high. Since Cas A is used as a calibrator source in the RING5M experiment, the OVRO observations of Cas A not only provide a corroborative check on the Saskatoon calibration, but can in principle refer the Saskatoon measurements to a flux density scale based on Jupiter, thereby reducing their calibration uncertainties to a few percent. Since Cas A is comparable in size to the 5.5-meter telescope beam, however, our measurement cannot be compared directly with the Saskatoon value, but must be multiplied by the factor

$$f = \frac{\int_{\Omega_{\rm cas}} P_{\rm Cas}(\theta,\phi) d\Omega}{\int_{\Omega_{\rm cas}} P_{\rm cas}(\theta,\phi) P_{\rm ovro}(\theta,\phi) d\Omega}, \tag{8}$$

where $P_{\rm cas}(\theta,\phi)$ is the source brightness distribution, and $P_{\rm ovro}(\theta,\phi)$ is the normalized antenna power pattern, given by the central lobe in Figure 1.

The correction factor in Eq. 8 was determined from a 32 GHz map of Cas A, made with the 100-m Effelsberg telescope (Morsi 1997, private communication), as a template for $P_{\rm cas}(\theta,\phi)$. The effect of uncertainties in the 5.5-meter telescope pointing, as well as in the determination of the telescope beam, was modeled via Monte Carlo simulation. Gaussian-distributed pointing positions were generated for 10^5 events, with $\sigma_A = \sigma_Z = 0'.3$ (typical for both telescopes) centered on the nominal pointing position; beamwidths were drawn from Gaussian distributions centered on the best-fit $\theta_{\rm min}$ and $\theta_{\rm maj}$. The 68% confidence interval of the resulting distribution for f is given by

$$f = 1.18^{+0.02}_{-0.01}. \tag{9}$$

With the flux density as seen by the OVRO 5.5-meter telescope beam given by $S'_{\rm ovro} = 164.18 \pm 5.45$ Jy (see Table 3), and accounting for the secular decrease in the flux density of Cas A since 1994 (Baars et al. 1977), application of Eq. 9 yields

$$S_{\rm ovro} = 195.59^{+7.29}_{-6.70} \text{ Jy}, \tag{10}$$

or

$$S_{\rm ovro} = (1.05 \pm 0.04) S_{\rm sask} \tag{11}$$

(Netterfield 1995), consistent with the Saskatoon calibration.

6. CALIBRATION

The power received from a source of specific intensity I uniformly filling the main beam Ω_m of the telescope power pattern is given by

$$P = \frac{1}{2} I A_p \eta_a \Omega_m \Delta\nu, \tag{12}$$

where η_a is the ratio of the effective aperture of a dish to its physical aperture A_p, known as the *aperture efficiency*. The power in instrumental units is converted to physical units by comparison with the power emitted by a calibrator source of known intensity $I_{\rm cal}$, typically a noise diode internal to the receiver. Since the radiation from an internal noise diode fills the beam solid angle Ω_a of the telescope, the ratio $P/P_{\rm cal}$ is given by

$$\frac{P}{P_{\rm cal}} = \frac{I\Omega_m}{I_{\rm cal}\Omega_a} \equiv \frac{I\Omega_m}{S_{\rm cal}}, \tag{13}$$

so that the intensity for a source filling the main beam is given by

$$I = \left(\frac{P}{P_{\rm cal}}\right)\frac{S_{\rm cal}}{\Omega_m}. \tag{14}$$

Atmospheric attenuation reduces the observed intensity of a source by a factor $\kappa(Z) = \exp(-\tau A(Z))$, where τ is the atmospheric opacity at zenith and $A(Z) \simeq \sec(Z)$ is the airmass. Thus, to recover the intensity of a source above the atmosphere, we must compute

$$I_0 = \left(\frac{P}{P_{cal}}\right)\left(\frac{S_{cal}}{\Omega_m}\right)\frac{1}{\kappa(Z)}. \tag{15}$$

Throughout this paper, we will alternately use *intensity* I, *brightness temperature* T_B (the equivalent Rayleigh-Jeans (R-J) temperature of a source filling the main beam Ω_m) and *antenna temperature* T_A (the equivalent R-J temperature of a source filling the beam solid angle Ω_a). These are related simply by

$$I\Omega_m = \frac{2kT_B}{\lambda^2}\Omega_m = \frac{2kT_A}{\lambda^2}\Omega_a, \tag{16}$$

whence

$$T_B = \frac{T_A}{\eta_b}, \tag{17}$$

where $\eta_b \equiv \Omega_m/\Omega_a$.

The mean 31.7 GHz zenith atmospheric opacity at the OVRO during 1996 is determined by fits to the daily calibrator source observations, yielding $\overline{\tau}_{31.7} = 0.045 \pm 0.002$, consistent with the mean annual zenith opacity estimated from a water vapor radiometry (WVR) system at the OVRO during 1994-1996. The error in I_0 introduced by adopting a constant mean opacity during 1994-1996 is $< 0.02\%$ (Leitch 1998). Extrapolation to 14.5 GHz of WVR opacities measured at 31.4 and 20 GHz yields $\overline{\tau}_{14.5} = 0.023$.

Maps of the main beam, shown in Figure 1, were obtained in 1995 from raster-scans across Jupiter and 3C 84 (for the $7'.4$ beam, Jupiter is approximately a point source). At 14.5 GHz, scans were restricted to lie within $\pm 5^\circ$ of $Z_{\rm Ring}$ so that the resulting beam map is the one appropriate for calibration of the RING5M data (see §2). At both frequencies, the main beam solid angle Ω_m is determined to an accuracy of $\leq 1\%$.

As discussed in §5, three independent estimates of the noise diode flux density $S_{\rm cal}$ were obtained each day during 1996, from which we deduce that the intrinsic output of the diodes at 31.7 GHz varies by $\leq 1\%$. At 14.5 GHz, instrumental effects resulted in a variation of $\leq 2\%$ in the diode power output. In the Rayleigh-Jeans regime,

$$S_{\rm cal} = \frac{2kT_{\rm cal}}{\lambda^2}\Omega_a, \tag{18}$$

so that the flux density of the diodes can also be determined by measuring the diode antenna temperature. These measurements are performed in the standard manner by comparison with external loads of known temperature and form the basis of our calibration prior to 1996, when calibrator sources were not observed on a regular basis. The uncertainty in the diode temperature determined from these measurements, when combined in quadrature with the error in the non-linearity correction (see §4), is 3.2%. Note, however, that this calibration method requires a separate measurement of Ω_a from Eq. 18, so that uncertainties in the temperature scale enter twice if Ω_a and $T_{\rm cal}$ are not determined simultaneously.

At 31.7 GHz, the first calibration method yields

$$\sigma_I^2/I^2 = (0.6\%)^2_{\Omega_m} + (3.3\%)^2_{S_{\rm cal}}, \tag{19}$$

for a total calibration uncertainty of 3.4% from 1996, while the second gives

$$\sigma_I^2/I^2 = (0.6\%)^2_{\Omega_m} + (3.5\%)^2_{\Omega_a} + (3.2\%)^2_{T_{\rm cal}}, \tag{20}$$

or a total calibration uncertainty of 4.7% prior to 1996. At 31.7 GHz, the mean of the calibration errors from the three independent seasons (see below), weighted by the measurement error in the variance from each season, gives a total calibration uncertainty of

$$\sigma_{I\,31.7\ {\rm GHz}} = 4.3\%. \tag{21}$$

7. DATA SELECTION

On the 5.5-meter telescope, a total of three seasons of data were obtained at 31.7 GHz from the winter of 1993 to the spring of 1996. A typical observing season at the OVRO lasts from early October until mid May. On the 40-meter telescope, construction of the 14.5 GHz receiver was completed in the spring of 1994, and only two seasons of data were obtained. Due to procedural differences in observing strategy between the first and second halves of 1996, however, these data are divided into two seasons which are analyzed separately below (for details, see Leitch 1998).

7.1. *Miscellaneous Edits*

The first level of FLUX editing consists of rejecting all data taken when the receiver was saturated during periods of high atmospheric water content. Since the receiver typically remains saturated during all four segments of the FLUX procedure (see §3), these are readily identified as data with standard deviations identically zero. This rejects less than 1% of the data. Next, data taken during excessively windy conditions, leading to tracking errors,

are identified by the excess time taken for a FLUX procedure to complete. Any data for which the difference between the actual and expected duration is $> 1^s$ are excised, eliminating between $1-10\%$ of the data. The range indicates the spread between the three major divisions of data at each frequency, described above.

The non-linearity correction discussed in §4 requires interpolation of the total power onto the FLUX data. Any FLUX for which no bracketing power measurements are found within 1^h is rejected, typically affecting 1% or less of the data. No non-linearity correction is applied to the 14.5 GHz data, as both CALs and FLUXes are measured against the sky, and thus against the same power background.

7.2. *Statistical Edits*

The noise diodes are sampled every 15 minutes to remove gain fluctuations from the data. The scatter in these diode measurements therefore provides an unbiased criterion for culling data affected by rapid gain variations on both telescopes, and by atmospheric fluctuations on the 40-meter telescope. (Diodes at 14.5 GHz are measured directly against the sky, while diodes on the 5.5-meter telescope are measured against internal loads, reducing the contribution of atmospheric fluctuations to scatter in the CALs by a factor of ~ 100.) In this step, $4-12\%$ of the data at 31.7 GHz and $14-40\%$ of the data at 14.5 GHz are rejected.

Next, a series of statistical edits are applied to the data. These have previously been described in Myers et al. (1997), and the same notation is retained here for consistency. A combination of sliding buffer edits is implemented, where in each case we form the test statistic

$$t_i = X_i/\sigma_{i_{th}}, \tag{22}$$

where the data X_i have been divided by $\sigma_{i_{th}}$, the expected thermal noise for the i^{th} measurement ($\sigma_{\rm rms} = 1.4$ mK s$^{1/2}$ at 31.7 GHz, and $\sigma_{\rm rms} = 2.3$ mK s$^{1/2}$ at 14.5 GHz). The tested quantity X can be the SD or SW, a combination of the A-D integrations (see §3) which cancels the signal in the far field, used to reject data during periods of high residual atmospheric or instrumental fluctuations (see Myers et al. 1997, Leitch 1998). Successive buffers of N points are constructed in time, where the width of the buffer is constrained to be no more than two hours. For each buffer j, we compute the mean

$$\overline{t}_j = \frac{1}{N}\sum_{i=j}^{j+N-1} t_i, \tag{23}$$

and standard deviation

$$\sigma_j = \left[\frac{1}{N-1}\sum_{i=j}^{j+N-1}(t_i-\overline{t}_j)^2\right]^{1/2}. \tag{24}$$

A point is rejected if there exists no buffer containing that point for which either $\overline{t}_j < \overline{t}_{max}$ or $\sigma_j < \sigma_{max}$, designated "meanX[N, $\overline{t}_{max}$]" and "sigX[N, σ_{max}]," respectively. These filters are applied to the combined data from all RING5M fields, as their primary purpose is to reject data affected by the atmosphere, regardless of the field being observed. In addition to these buffer edits, we employ a simple point-by-point filter which rejects data for which $t_i > t_{max}$, designated "X[t_{max}]."

A final edit, and the only edit in which the FLUX data themselves are used as a rejection criterion, is an iterative, field-by-field 4σ outlier rejection. This serves to reject isolated spurious signals due to local radio-frequency interference, and typically affects $< 0.5\%$ of the data. The combined edits reject 50% of the data at 31.7 GHz and 40% at 14.5 GHz and are summarized in Table 4.

The effect of the editing on the weighted field means (see §7.3) was investigated by reducing the data for a wide range of editing parameters; the mean standard deviation per field introduced by varying the cutoffs is found to be < 4 μK (see Figure 5).

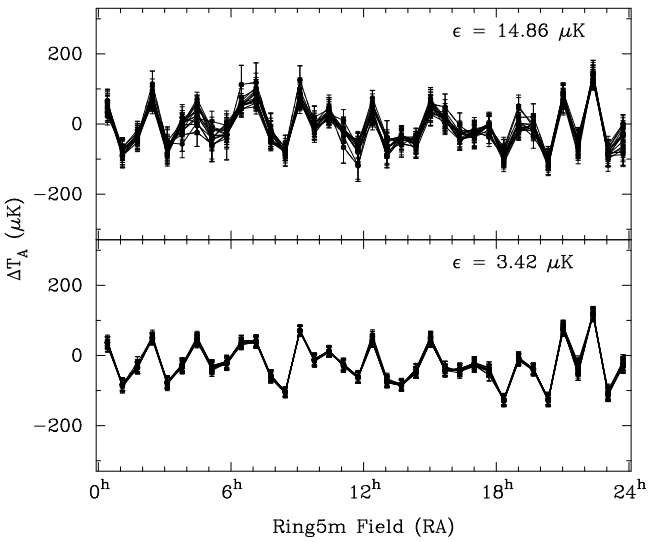

FIG. 5.— Reduction of the 1994 RING5M 31.7 GHz data for 15 editing schemes for unweighted means (top panel), and the same reductions using weighted means (bottom panel). Even in the case of the unweighted editing schemes, the mean standard deviation per field (shown at the top right of each plot) is smaller than the statistical error bars, and in the case of the weighted data, is practically negligible.

At 31.7 GHz, measurements of the noise diodes against the internal loads can be used to estimate the residual contribution of the atmosphere to the filtered data standard deviations; while the distribution of diode SDs is consistent with the expected thermal noise, the distribution of FLUX SDs against the sky peaks at 1.4 times the thermal limit, with a considerable skew to higher SDs. We attribute this excess noise to residual atmospheric fluctuations not removed by the fast switching (recall that on the 5.5-meter telescope, the ANT and REF beams depart significantly beyond ~ 0.5 km, while the typical scale height of water vapor is ~ 2 km). At 14.5 GHz, the peak of the FLUX SD distribution is within 10% of the thermal limit, consistent with the lower atmospheric opacity at 14.5 GHz and the better overlap of the 40-meter telescope beams.

7.3. *Field Means*

Data for each RING5M field are acquired in 40-minute scans, during which ~ 21 double-switched FLUXes are collected. After the data filtering described in §7.1-§7.2, the

TABLE 4
DATA EDITS

	31.7 GHz			14.5 GHz		
Edit[a]	1994	1995	1996	1995	1996_1	1996_2
Saturated (%)	0.05	0.77	0.15	0.20	0.64	0.03
Outlier (%)	0.46	0.24	0.14	0.21	0.15	0.37
No Powers (%)	0.69	1.41	0.00	0.00	0.00	0.00
SD[2.5] (%)	1.87	1.77	2.34	2.34	1.92	2.72
sigSW[25,7.5] (%)..	2.25	1.67	2.07	0.02	0.00	0.00
CALs (%)	3.99	4.06	11.39	24.61	39.80	13.58
Excess time (%) ...	9.72	1.00	3.92	24.60	1.29	3.67
meanSD[25,2.0] (%)	22.64	36.87	35.53	3.16	1.11	1.38
Total rejected (%) .	41.67	47.78	55.53	55.13	44.91	21.75
Total[b].....	68,359	98,617	107,494	32,743	29,209	40,584

NOTE. — Percentage figures are percent of data points that were rejected.

[a]For an explanation of notation, see §7.

[b]Total number of data points before editing.

weighted mean $\overline{\Delta T}_i \pm \epsilon_i$ for each field i is computed as follows:

$$\overline{\Delta T}_i = \frac{1}{W_1}\sum_{j=1}^{N_i} w_{ij}\Delta T_{ij} \tag{25}$$

$$\epsilon_i^2 = \frac{W_2}{W_1^2}\sigma_i^2 \tag{26}$$

$$\sigma_i^2 = \frac{N_i}{N_i-1}\frac{1}{W_2}\sum_{j=1}^{N_i} w_{ij}^2(\Delta T_{ij} - \overline{\Delta T}_i)^2 \tag{27}$$

$$W_1 = \sum_{j=1}^{N_i} w_{ij} \tag{28}$$

$$W_2 = \sum_{j=1}^{N_i} w_{ij}^2, \tag{29}$$

where ΔT_{ij} is the double-switched temperature from a single FLUX procedure (see §3), and N_i is the total number of FLUXes recorded for field i. Formally, the weights w_{ij} should be chosen so that the sample mean is a maximum likelihood estimator for the mean of the underlying distribution, i.e., $w_{ij} = \sigma_{ij}^{-2}$. In general, however, the standard deviation σ_{ij} reported with each datum (typically 1.4 × the thermal noise at 31.7 GHz) underestimates the scan standard deviation by a factor of 2-3, presumably due to atmospheric fluctuations on timescales longer than a single FLUX measurement. The scan variance $\sigma^2_{ij\,\mathrm{sc}}$ is thus a better estimate of the real error, and we take $w_{ij} = (\sigma_{ij}^2 + \sigma^2_{ij\,\mathrm{sc}})^{-1}$ when computing statistics for the RING5M fields.

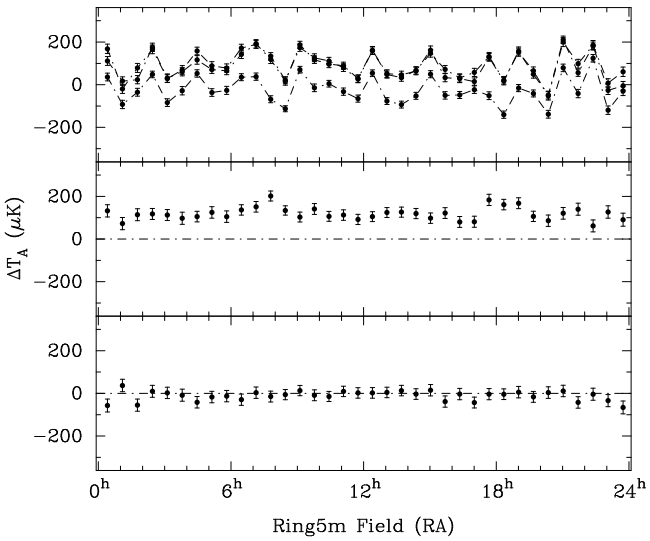

FIG. 6.— RING5M results for 1994-1996. (Top panel) Three years of data, with no means subtracted. Subtraction of the 1994 and 1995 data sets (middle panel) shows that the Ring has changed by a constant offset ($\Delta T = 119.41$ μK, $\chi_r^2 = 1.34$), while the 1996 and 1995 data sets are consistent with no change ($\Delta T = -9.93$ μK, $\chi_r^2 = 0.71$) (bottom panel).

7.4. *Mean Levels*

The 31.7 GHz RING5M field means for 1994 – 1996 are shown in Figure 6. Between 1994 and 1995, the mean level of the Ring changed by approximately 120 μK, while between 1995 and 1996, the difference is consistent with zero. Subtraction of the data sets shows that in each case the shift is consistent with an offset which is constant from field to field and thus does not affect our estimate of the sky variance (a variable point source contributes to the measured signal in the first field (see §10), which affects the two neighboring fields through the double switching). The constancy of these offsets implies that they are instru-

mental in origin.

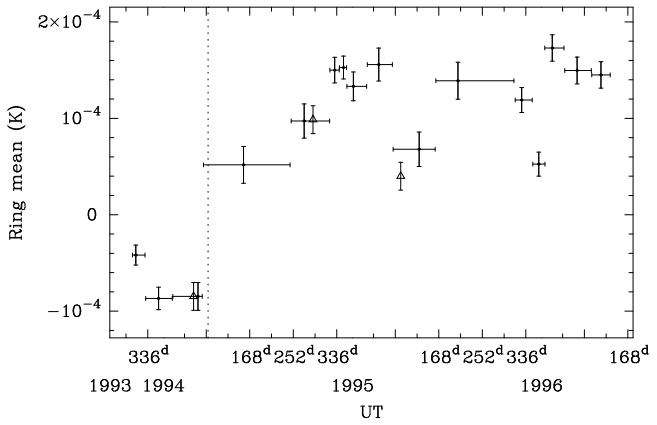

FIG. 7.— Mean levels for the 31.7 GHz Ring data, 1994-1996, where bins contain equal numbers of data points. The large step in the mean level coincides with a HEMT change on day 91, 1994 (indicated by the dotted line). Assuming variations in the mean are given by Eq. 5, the predicted mean of the Ring at the two epochs in 1994 and 1995 when measurements of the directional isolations were made are indicated by open triangles, normalized to the mean observed in 1993.

Figure 7 shows that the largest shift in the mean level occurred after a HEMT changeover on day 91 of 1994. In §4, we showed that a mismatch in the directional isolations of the Dicke switch can lead to incomplete cancellation of ground or atmospheric temperature gradients. Replacement of the HEMT will undoubtedly change the impedance at the output port of the switch, quite likely resulting in a change in isolation. At 31.7 GHz, three measurements were made of the isolations, one before the HEMT changeover, and two after. We find that when the error term given by Eq. 5 is normalized to the RING5M mean in 1993, the mean levels predicted by the isolations measured in 1994 and 1995 (shown as open triangles in Figure 7) are in excellent agreement with the data; in each case the predicted and measured mean levels agree to within errors and imply a constant temperature gradient of $\Delta\phi\frac{\partial T}{\partial\phi} = -16$ mK across the beamthrow of the telescope.

8. CONCORDANCE

Edited and calibrated means for the 36 fields, representing a combined total of approximately 4,500 hours of data, are shown in Figure 8. A mean level has been subtracted from each season. Within each season, we test for internal consistency by dividing the data set into two halves in time. While the time spanned by a given season is insufficient to permit a sensible comparison of data taken at night to data taken during the day (see §7), the data are nevertheless quite repeatable on timescales over which the field positions have precessed significantly relative to the Sun; linear correlations (Pearson's r) between halves fall in the range $r_{\rm obs} = 0.72 - 0.89$.

At both frequencies, the data show structure well above the noise and repeatable from year to year. At 31.7 GHz, the season-to-season deviations in the field means are Gaussian, and correlations between seasons are $r_{\rm obs} \geq 0.89$. The probability of observing correlations this high under the hypothesis that the sky temperatures are uncorrelated is $p(r > r_{\rm obs}) \leq 6 \times 10^{-8}$. Under the hypothesis that the data are completely correlated, as we should expect if the signals are dominated by the microwave background, these correlations fall within the 68% confidence region for $r_{\rm obs}$, given typical season-to-season field errors of ~ 20 μK (antenna temperature). Because of the double switching, the RING5M field means are not statistically independent; all probabilities quoted in this paper take the effect of the switching into account. In addition, we assume that the unswitched sky temperatures are drawn from a Gaussian distribution.

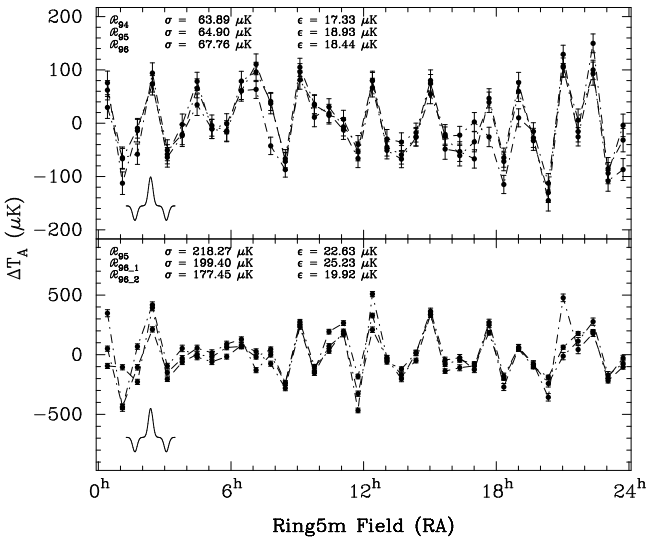

FIG. 8.— RING5M 31.7 GHz (top) and 14.5 GHz (bottom) field means (antenna temperature) from winter of 1993 ($\mathcal{R}_{94}$) to winter of 1995 ($\mathcal{R}_{96}$). The rms is denoted σ, and ϵ is the mean error per field. At bottom left is the beam pattern produced by the double switching, i.e., the effective point-spread function for the OVRO telescopes.

At 14.5 GHz, the agreement is also good, with the exception of the RING5M field at $21^{\rm h}04^{\rm m}$ (OV5M2104), in which an anomalously high (and to date unexplained) signal was seen during the first half of the 1995 season, and OV5M0024, which is dominated by a bright variable point source (see §10). The two fields adjacent to OV5M0024 are affected by the same point source due to the double switching. These effects collectively reduce season-to-season correlations at 14.5 GHz to the range $r_{\rm obs} = 0.72 - 0.87$.

9. TERRESTRIAL CONTAMINATION

Since the features we detect at both frequencies are fixed in sidereal time, local radio frequency interference (RFI) is an unlikely explanation for the structure observed in the RING5M data. Nonetheless, if there is ground-based interference, the change in telescope elevation as a field is tracked through transit will introduce a characteristic parallactic angle dependence into the data for any one field (see §5.1), and we can look for this signature in the RING5M data.

The means for all 36 fields are shown in Figure 9, binned in parallactic angle. We find no parallactic angle dependence in the 31.7 GHz data, indicating that these data are free from RFI contamination. The 14.5 GHz data, on the other hand, show a large variation in amplitude with parallactic angle, indicating significant contamination. This

pattern, however, occurs with the same amplitude in each field (Figure 9 is a compilation of data from all 36 RING5M fields), demonstrating that RFI contributes only a mean level, constant over long timescales, so that our measurement of the variance should be unaffected.

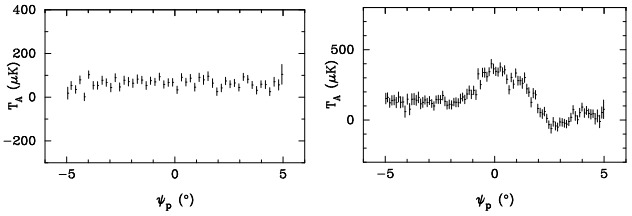

FIG. 9.— Co-added 31.7 GHz (top) and 14.5 GHz (bottom) data from all 36 RING5M fields, binned in parallactic angle. The 14.5 GHz data show the characteristic signature of interference from the ground, while the 31.7 GHz data appear free of contamination.

Although the parallactic angle dependence is a good indicator of the robustness of our data to interference, we can definitively rule out terrestrial contamination as a source of *structure* at 14.5 GHz by observing the fields at lower culmination. Since this changes the position of the telescope beams only relative to the ground, signals from the sky will remain unaltered, while any time-dependent fluctuations from the ground will be shifted by 12 hours. This test was performed on 1996 Sep 16-30. (The strength of the signals at 14.5 GHz permits a reasonable detection in this relatively short time.) The comparison of the mean upper culmination 14.5 GHz data set with the lower culmination data is shown in Figure 10. Field errors are estimated by reducing the 1996 upper culmination data in 2-week subsets; the error in the mean for each field is typically about 62 μK in antenna temperature.

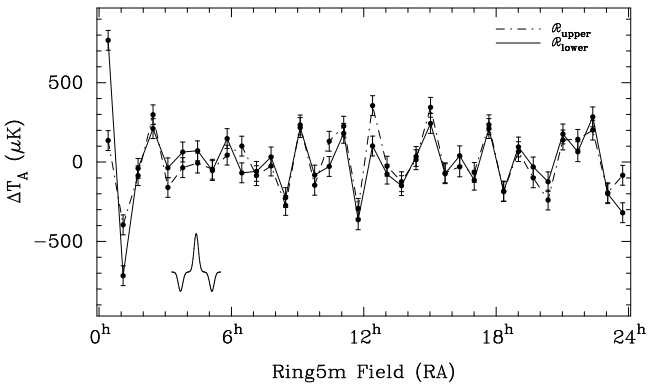

FIG. 10.— 14.5 GHz upper culmination field means (dot-dashed line), shown with the lower culmination data (solid line). The good agreement of these two data sets effectively rules out terrestrial RFI as the source of the observed structure in the Ring. The large differences in the first, second and last fields are due to discrete sources (see text). At bottom left is the effective beam pattern for double-switched observations.

The lower culmination data show the same structure, to within errors, as the upper culmination data, demonstrating that the origin of these signals is undoubtedly celestial. The large differences in fields OV5M0024, OV5M0104 and OV5M2344 are due in part to variability of a point source which dominates the signal in field OV5M0024, and to the slightly asymmetric 14.5 GHz double-switched beam pattern, which is inverted at lower culmination relative to the upper culmination beam.

10. DISCRETE SOURCES

Mosaicked VLA observations covering the RING5M fields to the 3% contour of the 7′.4 beam were made in 1994, with an rms sensitivity at 8.5 GHz of 0.21 mJy. The sensitivity of the 5.5-meter telescope to point sources is 4.1 mK Jy^{-1}, so that these observations allow detection of any source contributing $\gtrsim 13\,\mu$K (4σ) to our highest frequency data with an accuracy of $\lesssim 3\,\mu$K (1σ), assuming $\alpha \leq +1$ (where $S_\nu \propto \nu^\alpha$). During the period bracketing the 1996 RING5M season, we obtained multi-epoch VLA observations at 8.5 and 15 GHz of the 39 sources (56 discrete components in all) found in the original 8.5 GHz survey. These observations allow extrapolation of source flux densities to 31.7 GHz and removal of variable contributions to the RING5M data from sources which vary on timescales $\gtrsim 1$ month.

From October 1995 – May 1996, RING5M sources were observed at 11 separate epochs, in BnA, B, CnB, C and DnC configurations. Due to the time constraints of the 15 GHz observations (the approximate 10 minute sensitivity of the VLA at 15 GHz is 0.17 mJy, compared to 0.045 mJy at 8.5 GHz, so that 80% of our observing time was spent at 15 GHz), not all sources could be observed at each epoch. Sources which early-on showed significant variability were observed at each epoch, while any remaining sources which could not be observed at a given epoch were observed during the next. Typical rms noise in the maps was 0.25 mJy at 8.5 GHz and 0.5 mJy at 15 GHz.

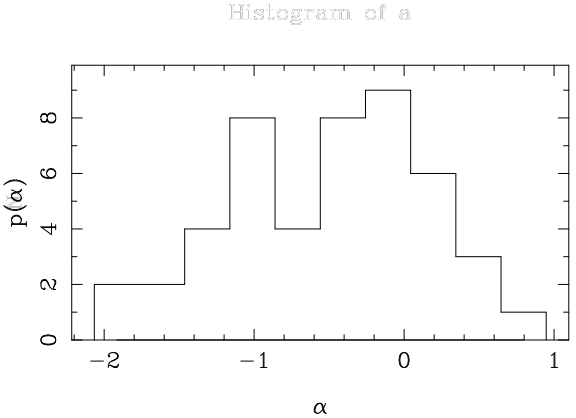

FIG. 11.— The histogram of spectral indices for sources selected at 8.5 GHz, derived from the 47 discrete source components detected at both 8.5 and 15 GHz. Here, $p(\alpha)$ is the number of sources with spectral index $\alpha \pm 0.15$.

For each source, the visibilities from all epochs at which the source was observed are combined to form a single high-sensitivity map at each frequency from which an accurate model for the source spatial structure can be determined. Several sources have multiple components, consisting of a core and one or two prominent lobes, while others show two point-like components closer than one would expect from random superpositions of unrelated sources. Model-fits to these combined maps also provide a measurement of the mean flux density at each frequency. These

are given in Table 5 for sources detected at both frequencies, along with the source flux densities extrapolated to 31.7 GHz.

Although sources detected at 8.5 GHz but not at 15 GHz — nine in all — have falling spectra and will contribute negligibly to the RING5M data, we can take a Bayesian approach (Sivia 1996) to estimate their flux densities at higher frequencies. The distribution of spectral indices for sources selected at 8.5 GHz, shown in Figure 11, is constructed from the 47 components detected at both 8.5 and 15 GHz. Once the distribution of spectral indices is known, the probability distribution of the 15 and 31.7 GHz flux densities, given the measured flux density at 8.5 GHz and an upper limit at 15 GHz, can be constructed for each source via Monte Carlo simulation, yielding the maximum likelihood estimates and corresponding 68% confidence intervals given in Table 5.

The estimated contribution of point sources to the 1996 31.7 and 14.5 GHz data is shown in Figure 12. Few of the sources are bright enough or close enough to a field center to contribute a significant signal, with the notable exception of a ~ 100 mJy source which dominates the signal in field OV5M0024 and affects the two adjacent fields through the double switching. If we exclude OV5M0024 and its flanking fields, the rms at 31.7 GHz due to discrete sources is $12\,\mu$K (antenna temperature), or $< 4\%$ of the observed variance, and $58\,\mu$K at 14.5 GHz, or $< 10\%$ of the variance observed there.

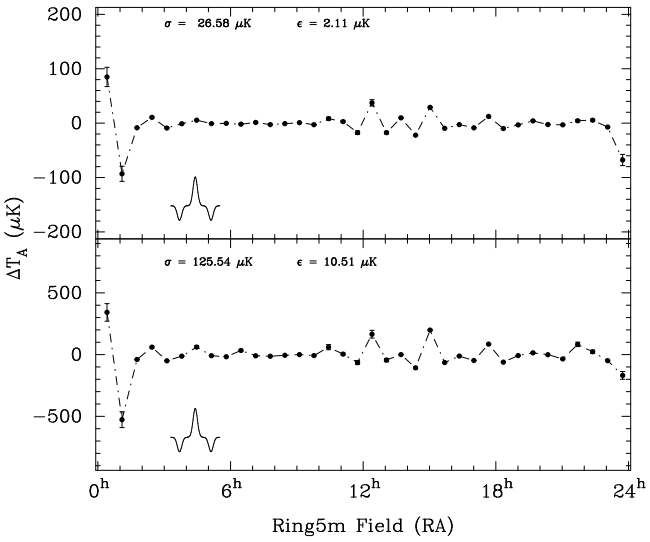

FIG. 12.— Point source contribution to the 31.7 GHz Ring data (top), and to the 14.5 GHz data (bottom), extrapolated from VLA monitoring at 8.5 and 15 GHz. Error bars reflect uncertainties in the source fluxes due to pointing only. At bottom left is the effective response to a point source near a Ring field center.

Because sources were monitored during 1996, formal errors from point source subtraction for this season are typically a few μK. Since many of the RING5M sources lie on the exponential cutoff of the $7'.4$ beams, however, small errors in pointing can produce large changes in the antenna temperature produced by a source, so that the variance due to pointing errors contributes significantly to the uncertainties. Field errors in Figure 12 are the computed standard deviations due to pointing, assuming Gaussian azimuth and zenith angle pointing errors with $\sigma_A = \sigma_Z = 0'.3$. At 31.7 GHz, the largest uncertainty due to pointing is 17 μK, while at 14.5 GHz, the largest error is 70 μK, comparable to the variance of the brightest variable source in the Ring, making pointing the dominant uncertainty. We assume this to be true even for years when the sources were not monitored.

In all subsequent analysis, a single combined data set is used at each frequency. Although the errors due to point-source subtraction are not comparable from year to year, we can define a mean error for each field

$$\sigma = \frac{\sum_j \sigma_j w_j}{\sum_j w_j}, \tag{30}$$

where σ_j is the error from source subtraction from season j, and w_j is the sum of the weights from season j, i.e.,

$$w_j = \sum_k^{N_j} 1/\epsilon_{jk}^2, \tag{31}$$

where ϵ_{jk} is the error in an individual FLUX measurement. To these we add in quadrature the statistical errors for each field mean and the error per field due to pointing uncertainties.

The mean source-subtracted R-J temperatures ΔT_i and associated uncertainties ϵ_i at each frequency are given in Table 6.

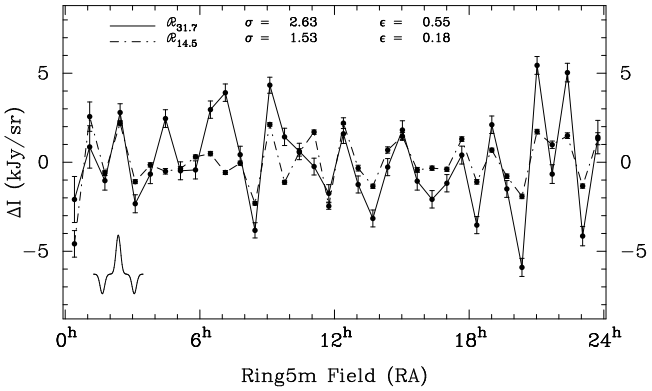

FIG. 13.— Mean source-subtracted 31.7 GHz (solid line) and 14.5 GHz (dotted line) RING5M data, to equal intensity scales. See Eq. 16 for the conversion from ΔI (kJy/sr) to ΔT_B (K).

11. FOREGROUNDS

Mean (1993–1996) source-subtracted data sets at each frequency are shown in Figure 13. The correlation between frequencies is remarkably high, with $r_{\rm obs} = 0.81$ and probability of observing a higher correlation than this under the hypothesis that the data are uncorrelated given by $p(r > r_{\rm obs}) = 2.7 \times 10^{-6}$. The good agreement between several years of data from two independent instruments demonstrates that the observed structure in the RING5M data must originate outside the telescopes. Furthermore, as discussed in §9, observations of the RING5M fields at lower culmination rule out interference from the ground. We are therefore confident that the signals are celestial in origin.

TABLE 5
SUMMARY OF SOURCE FLUX DENSITIES

α (J2000)	δ (J2000)	$\overline{S}_{8.5\ \mathrm{GHz}}$ (mJy)	$\overline{S}_{15\ \mathrm{GHz}}$ (mJy)[a]	$\overline{S}_{31.7\ \mathrm{GHz}}$ (mJy)[a]
00:22:12.97	87:53:56.64	2.10 ± 0.10	$0.78^{+0.16}_{-0.06}$	$0.20^{+0.11}_{-0.04}$
00:32:41.48	87:50:43.61	89.86 ± 0.56[b]	107.08 ± 0.49	126.44 ± 0.60
02:22:09.58	87:52:18.73	4.14 ± 0.10	3.67 ± 0.26	3.12 ± 0.27
02:31:45.60	87:49:10.76	4.49 ± 0.10	5.03 ± 0.34	5.85 ± 0.47
04:28:27.47	87:58:32.65	17.89 ± 0.15	9.75 ± 0.31	4.33 ± 0.15
06:30:29.55	87:53:18.41	1.84 ± 0.11	$0.69^{+0.19}_{-0.06}$	$0.18^{+0.14}_{-0.04}$
06:30:29.55	87:53:19.64	0.66 ± 0.11	$0.32^{+0.17}_{-0.10}$	$0.09^{+0.22}_{-0.05}$
06:34:14.18	87:56:23.83	2.78 ± 0.11	$1.01^{+0.14}_{-0.06}$	$0.26^{+0.09}_{-0.04}$
07:02:43.09	87:45:09.00	7.67 ± 0.12[b]	7.84 ± 0.40	8.07 ± 0.46
08:56:31.32	87:47:58.19	1.70 ± 0.11	2.10 ± 0.28	2.79 ± 0.53
09:38:58.18	87:50:52.59	2.23 ± 0.12	$0.84^{+0.13}_{-0.09}$	$0.22^{+0.10}_{-0.05}$
10:18:52.68	87:56:08.52	8.32 ± 0.09	5.97 ± 0.42	3.83 ± 0.27
10:20:12.52	87:56:11.76	5.51 ± 0.09	4.87 ± 0.37	4.13 ± 0.37
10:21:12.46	87:56:00.62	22.67 ± 0.09	17.13 ± 0.41	11.78 ± 0.27
10:56:50.10	87:47:46.16	5.19 ± 0.10	5.97 ± 0.33	7.76 ± 0.48
11:46:15.05	87:54:55.13	4.88 ± 0.08	3.59 ± 0.29	2.38 ± 0.24
11:46:13.76	87:54:56.52	0.99 ± 0.08	$0.39^{+0.15}_{-0.05}$	$0.11^{+0.12}_{-0.04}$
11:48:37.64	87:42:05.72	13.13 ± 0.12[b]	5.86 ± 0.30	1.99 ± 0.12
11:48:39.63	87:42:09.74	2.62 ± 0.12[b]	0.87 ± 0.30	0.20 ± 0.12
11:53:24.39	87:56:06.25	7.07 ± 0.10	3.94 ± 0.30	1.80 ± 0.17
12:11:50.52	87:50:54.44	11.88 ± 0.32	12.72 ± 0.31	13.94 ± 0.39
12:16:17.38	87:51:24.27	20.45 ± 0.23[b]	21.36 ± 0.31	18.76 ± 0.31
12:55:57.99	87:48:00.82	3.72 ± 0.10	3.66 ± 0.27	3.58 ± 0.33
13:00:16.65	87:45:09.98	9.16 ± 0.11	5.10 ± 0.30	2.33 ± 0.16
13:41:49.23	87:48:20.03	1.89 ± 0.09	2.99 ± 0.29	5.52 ± 0.70
14:27:16.54	87:47:39.89	4.70 ± 0.16[b]	3.18 ± 0.26	1.89 ± 0.20
14:33:37.94	87:51:07.58	2.91 ± 0.11	$1.06^{+0.11}_{-0.07}$	$0.27^{+0.08}_{-0.04}$
15:00:10.90	87:50:53.45	6.17 ± 0.13	3.74 ± 0.61	1.92 ± 0.38
15:00:10.12	87:50:57.62	3.91 ± 0.13	3.30 ± 0.61	2.63 ± 0.60
14:59:50.43	87:50:07.46	4.68 ± 0.13	4.21 ± 0.72	3.65 ± 0.63
15:02:54.05	87:58:44.39	3.07 ± 0.12	1.90 ± 0.38	1.00 ± 0.28
15:11:29.40	87:55:43.30	1.91 ± 0.11	2.29 ± 0.39	2.92 ± 0.68
15:11:34.96	87:55:46.31	1.24 ± 0.11	$0.49^{+0.21}_{-0.06}$	$0.14^{+0.17}_{-0.05}$
15:42:38.53	87:55:38.92	4.39 ± 0.10	3.30 ± 0.31	2.25 ± 0.26
17:03:23.72	87:45:10.68	5.01 ± 0.09	4.61 ± 0.30	4.12 ± 0.32
17:30:38.61	87:54:12.72	6.12 ± 0.13	2.21 ± 0.25	0.57 ± 0.09
17:31:05.73	87:54:12.77	2.46 ± 0.13	1.37 ± 0.25	0.63 ± 0.18
17:30:37.89	87:54:16.49	4.85 ± 0.13	3.79 ± 0.26	2.73 ± 0.22
17:31:04.27	87:56:33.13	2.19 ± 0.24	$0.83^{+0.29}_{-0.10}$	$0.23^{+0.21}_{-0.09}$
17:39:48.20	87:49:52.79	4.05 ± 0.08	3.99 ± 0.31	3.91 ± 0.37
17:45:23.55	87:44:33.37	15.29 ± 0.13[b]	11.26 ± 0.28	7.48 ± 0.20
19:00:58.12	88:01:38.76	6.80 ± 0.12[b]	3.59 ± 0.36	1.53 ± 0.19
19:29:34.27	87:55:02.19	3.07 ± 0.09	3.96 ± 0.27	5.56 ± 0.47
19:41:43.37	87:46:35.91	2.55 ± 0.11	3.21 ± 0.38	4.37 ± 0.66
20:32:28.60	87:59:24.91	13.96 ± 0.15	6.57 ± 0.28	2.40 ± 0.12
20:32:49.85	87:59:31.15	3.79 ± 0.15	2.24 ± 0.28	1.11 ± 0.19
20:32:52.51	87:59:25.76	2.87 ± 0.15	1.19 ± 0.28	0.37 ± 0.14
20:32:30.54	87:59:30.94	2.38 ± 0.15	2.01 ± 0.28	1.60 ± 0.32
21:41:01.80	87:58:10.62	3.50 ± 0.07	1.45 ± 0.27	0.45 ± 0.12
21:41:53.75	87:57:51.41	1.65 ± 0.07	1.54 ± 0.30	1.40 ± 0.35
21:41:52.32	87:57:53.02	4.31 ± 0.07	1.98 ± 0.29	0.70 ± 0.13
21:41:03.45	87:58:10.02	5.59 ± 0.07	3.80 ± 0.27	2.27 ± 0.19
21:41:41.22	87:57:55.77	2.02 ± 0.07	0.99 ± 0.28	0.38 ± 0.17
22:28:10.05	87:50:37.98	9.02 ± 0.09	8.82 ± 0.30	7.98 ± 0.31
23:16:20.13	87:49:41.46	7.71 ± 0.99	3.97 ± 0.41	1.63 ± 0.25
23:17:25.40	87:52:58.42	17.73 ± 0.15[b]	13.11 ± 0.30	8.77 ± 0.22

[a] Asymmetric errors indicate a source was not detected at 15 GHz and is a maximum likelihood estimate (see §10).

[b] Variable source.

TABLE 6
SOURCE-SUBTRACTED RING FIELD MEANS[a]

Field	$\overline{\Delta T}_{31.7}$ (μK)	$\epsilon_{31.7}$ (μK)[b]	$\overline{\Delta T}_{14.5}$ (μK)	$\epsilon_{14.5}$ (μK)[b]
OV5M0024	−67.78	36.88	−710.82	101.57
OV5M0104	27.95	32.78	397.69	96.38
OV5M0144	−33.59	17.15	−94.52	20.86
OV5M0224	90.73	15.94	339.78	21.75
OV5M0304	−75.61	16.40	−168.44	17.31
OV5M0344	−21.54	17.35	−23.06	18.68
OV5M0424	79.59	16.14	−78.56	24.04
OV5M0504	−15.49	16.32	−56.43	18.36
OV5M0544	−13.89	16.51	47.66	16.77
OV5M0624	95.96	15.75	75.63	18.99
OV5M0704	126.83	15.91	−89.17	17.21
OV5M0744	13.87	15.31	−7.65	17.91
OV5M0824	−124.12	13.88	−357.49	15.46
OV5M0904	140.53	14.57	329.81	15.61
OV5M0944	46.24	15.79	−174.36	16.63
OV5M1024	19.74	15.01	86.55	32.74
OV5M1104	−7.82	15.29	262.51	19.28
OV5M1144	−56.77	15.92	−381.74	27.99
OV5M1224	51.82	17.35	340.51	45.91
OV5M1304	−40.51	15.47	−50.77	25.38
OV5M1344	−102.35	15.40	−208.90	18.50
OV5M1424	−8.84	15.58	107.09	26.39
OV5M1504	58.72	16.95	225.55	35.13
OV5M1544	−34.40	16.27	−65.48	19.18
OV5M1624	−67.51	15.86	−51.07	18.61
OV5M1704	−38.27	15.76	−61.29	18.11
OV5M1744	13.11	16.33	201.98	20.53
OV5M1824	−114.55	15.50	−170.47	19.79
OV5M1904	68.41	16.03	105.79	17.35
OV5M1944	−48.60	15.31	−121.67	19.37
OV5M2024	−191.67	16.51	−297.43	19.70
OV5M2104	176.57	16.17	266.81	20.34
OV5M2144	−21.59	17.04	152.51	32.31
OV5M2224	163.50	16.90	231.69	24.88
OV5M2304	−134.58	17.65	−207.03	18.50
OV5M2344	45.92	27.35	204.82	47.56

[a]Equivalent R-J temperature.

[b]Errors are 1σ rms in the sample mean.

Since the CMBR specific intensity is approximately $I_{\rm cmb} = 2kT_{\rm cmb}\nu^2/c^2$, signals from the microwave background should be reduced at 14.5 GHz by a factor of ~ 5 relative to those at 31.7 GHz. As can be seen in Figure 13, however, many of the RING5M fields, notably in the regions $0^{\rm h} - 3^{\rm h}$ and $12^{\rm h} - 18^{\rm h}$, have equal intensities at the two frequencies, suggesting that the emission mechanism may be thermal bremsstrahlung. On the other hand, the regions $4^{\rm h} - 8^{\rm h}$ and $20^{\rm h} - 23^{\rm h}$ show the spectral signature of the CMBR.

The nature of the steep-spectrum (in temperature) signals seen in the RING5M data has been investigated by Leitch et al. (1997) (hereafter L1). There we used a maximum likelihood test (described in detail in §12) to rule out contamination by flat-spectrum foregrounds under the assumption that the CMBR is observed in the presence of a single foreground. We model the RING5M field means in the Rayleigh-Jeans regime as

$$\Delta T_{i\rm obs} = \Delta T_{i\rm cmb} + \Delta T_{i\rm fore}, \qquad (32)$$

where $\Delta T_{i\rm fore} \propto \nu^{\beta}$. Given two frequencies ν_1 and ν_2, we can eliminate the $\Delta T_{i\rm fore}$ and solve for the CMBR component in each field as a function of the unknown spectral index β;

$$\Delta T_{i\rm cmb}(\beta) = \frac{\Delta T_{i\rm obs}(\nu_1)\nu_1^{-\beta} - \Delta T_{i\rm obs}(\nu_2)\nu_2^{-\beta}}{\alpha(\nu_1)\nu_1^{-\beta} - \alpha(\nu_2)\nu_2^{-\beta}}, \qquad (33)$$

where $\alpha(\nu)$ is a factor which corrects for the R-J approximation to a true blackbody spectrum (at 31.7 GHz, $\alpha = 0.974$; see Leitch 1998). As can be seen in Figure 14, foregrounds with temperature spectral indices $\beta > -1.7$ can be ruled out at the 3σ level.

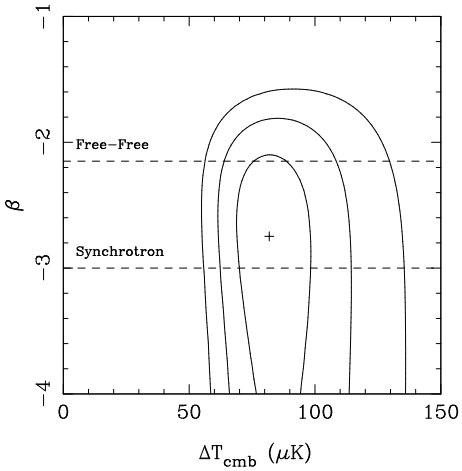

FIG. 14.— Likelihood function $\mathcal{L}(\Delta T_{\rm cmb}, \beta)$ (see §12) for the RING5M data, assuming CMBR + single foreground of temperature spectral index β. Plotted are the 68%, 95% and 99% highest probability density (HPD) intervals.

Although the RING5M data alone cannot provide much discrimination among the steepest spectral indices in a two-component model, since the CMBR component increasingly dominates for steeper foreground spectral indices, we can use low-frequency maps of the NCP to determine limits on the observed contribution of synchrotron emission to the RING5M data. At 325 MHz, maps from the WENSS survey (Rengelink et al. 1997) show no detectable signals (see Figure 15). As discussed in L1, we can use the rms in the 325 MHz map to rule out contamination of the RING5M data by any foreground with temperature spectral index $\beta < -2.2$.

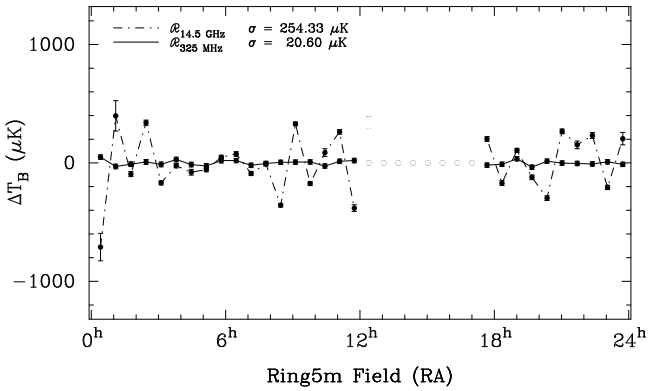

FIG. 15.— 14.5 GHz (dot-dashed line) and convolved 325 MHz map of the NCP (solid line) from the WENSS survey, extrapolated to 14.5 GHz assuming $\beta = -2.7$. Standard deviations are quoted for overlap region only (WENSS data are missing for fields OV5M1224 - OV5M1744). The comparison demonstrates that the structure observed at 14.5 GHz cannot be due to steep spectrum synchrotron emission.

If the 14.5 GHz structure is due to thermal bremsstrahlung emission, we would expect a considerable Hα signature, unless the temperature of the emitting gas is $T_e \gg 10^4$ K; lack of any detectable structure in Hα maps of the NCP in fact restricts the temperature of this component to $\gtrsim 10^6$ K (see L1 for details). In light of this, flat-spectrum synchrotron or non-thermal emission from dust (see below) may be a more likely explanation for these anomalous signals.

In L1, we also reported a significant correlation between the steep-spectrum foreground at 14.5 GHz and *IRAS* 100 μm emission near the NCP — independent confirmation that the structure observed in the Ring is celestial in origin (see Figure 16). Draine and Lazarian (1998) have recently suggested that non-thermal emission from spinning dust grains could produce emission with an apparent free-free spectrum, while naturally accounting for the observed correlation.

Thermal emission from the dust itself is not expected to be a serious contaminant at these frequencies (fits to the *COBE* DMR data on 7° scales suggest that $\sigma_{\rm dust} < 2$ μK at 31.4 GHz, while the DIRBE spatial template indicates that the power spectrum of the dust is falling as $\mathcal{P}(l) \propto l^{-3}$ with decreasing angular scale ($l \propto \theta^{-1}$); Kogut et al. 1996).

TABLE 7
RMS FOR MEAN 1994-1996 31.7 AND 14.5 GHZ DATA

	$\sigma_{31.7\ \mathrm{GHz}}$[a]	$\sigma_{14.5\ \mathrm{GHz}}$[a]
Raw	94.65 μK	249.93 μK
After point source subtraction.....	85.41 μK	238.06 μK
After foreground fitting, with $\beta_{\mathrm{fore}} = -2.2$	82.51 μK[b]	234.37 μK[c]

[a]R-J Temperature unless otherwise noted.

[b]CMBR Brightness Temperature.

[c]Extracted foreground component.

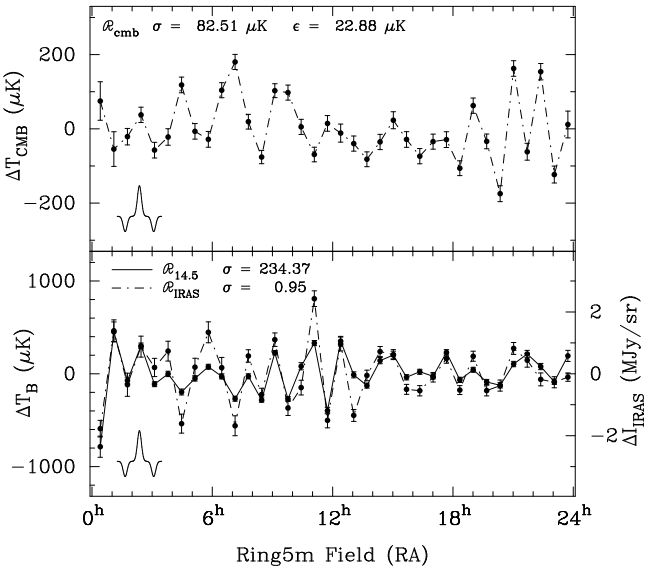

FIG. 16.— The extracted CMBR physical brightness temperatures (at 31.7 GHz) (top panel), and the extracted foreground equivalent brightness temperature (at 14.5 GHz) (bottom panel), assuming a spectral index $\beta = -2.2$. Note that at 14.5 GHz, even the regions $3^{\mathrm{h}} - 8^{\mathrm{h}}$ and $20^{\mathrm{h}} - 23^{\mathrm{h}}$, in which the CMBR dominates the combined signal (see Figure 13), now show a noticeable correlation with the *IRAS* 100 μm intensities.

12. INTRINSIC ANISOTROPY

In the foregoing discussion, we demonstrated that the signals detected in the RING5M experiment are consistent with a combination of steep spectrum ($\beta \sim -2.2$) and blackbody emission ($\beta \sim 0$), the former contributing 97% of the variance at 14.5 GHz, the latter responsible for 88% of the variance at 31.7 GHz. Low-frequency maps of the NCP were used to rule out contamination by $\beta < -2.2$ emission, leaving us with a foreground which either *is* free-free, or has very nearly the same spectral dependence, in either case justifying the assumption of a single foreground and allowing separate reconstruction of the CMBR and foreground components from linear combinations of the 14.5 and 31.7 GHz data (see Figure 16).

Although the unexpected correlation of the 14.5 GHz data with Galactic IR cirrus suggests that subtraction of a scaled IRAS template might be a viable method of extracting the CMBR component, we feel that this is not justified; CMBR plus a single foreground with the IRAS spatial template is a bad fit to our multifrequency data (best fit $\chi^2_r \simeq 10$), as can also be seen by the large residual differences in the lower panel of Figure 16. Furthermore, other methods which lead to more restrictive limits on the CMBR amplitude make unjustifiable assumptions about the distribution of the foreground. We therefore take the extraction outlined in the previous section to be the most conservative, as it makes only the assumption that the frequency depedence of the foreground can be modeled by a simple power law.

The approach we take to estimating the CMBR variance is the standard approach of Maximum Likelihood estimation (see, e.g., Sivia 1996). We assume that the 36 field means are drawn from a Gaussian distribution[3] on the sky, so that the joint probability of the data set is given by

$$\mathcal{L} = \frac{\exp(-\frac{1}{2}\mathbf{t}^T\mathbf{C}^{-1}\mathbf{t})}{(2\pi)^{N/2}\,|\mathbf{C}|^{1/2}}, \tag{34}$$

where $\mathbf{t}$ is the data vector, with elements ΔT_i given by Eq. 33, and $\mathbf{C}$ is the associated 36×36 covariance matrix. In general, the elements of $\mathbf{C}$ can be written

$$C_{ij} = \sigma^2_{ij} + C_{ij\,\mathrm{cmb}}, \tag{35}$$

where the σ^2_{ij} are the temporal covariances from the data (the diagonal elements σ^2_{ii} are just the variances of the field means). The $C_{ij\,\mathrm{cmb}}$ describe the predicted spatial variance from the CMBR, and in general are given by the 2-pt correlation of the effective antenna pattern convolved with the sky temperature field (see §13).

Once the likelihood function $\mathcal{L}(\Delta T_{\mathrm{cmb}}, \beta)$ is constructed for the CMBR component, our estimate of the CMBR variance $\Delta T^2_{\mathrm{cmb}} \equiv C_{ii\,\mathrm{cmb}}$ is obtained by maximizing $\mathcal{L}$ with respect to ΔT_{cmb}. Implicit in this construction is the assumption of a spectral index β for the anomalous foreground; note however, that even if all of the signal at 14.5 GHz were foreground, the relative contribution of this foreground to the total variance at 31.7 GHz is less than 25% for spectral indices as flat as $\beta = -2.2$ (see Table 7). Thus our estimate of the CMBR variance is not strongly

[3]Note that the Gaussian approximation is equivalent to retaining the first three terms in the Taylor expansion of any arbitrary distribution about its maximum.

dependent on the exact choice of foreground spectral index, as can also be seen from Figure 14.

A conservative approach is simply to integrate out the dependence of the likelihood on β, i.e.,

$$\mathcal{L}(\Delta T_{\rm cmb}) = \int \mathcal{L}(\Delta T_{\rm cmb}, \beta) d\beta, \tag{36}$$

where we restrict the integration to bounds defined by a reasonable prior, e.g., one uniform for $-3 < \beta < 2$, since no Galactic foregrounds are known with $\beta < -3$ (see Reich & Reich (1988), who find that the low-frequency radio spectral index near the NCP is ~ -2.7, and Banday & Wolfendale (1991), who present evidence that the synchrotron spectral index steepens to $\beta \sim -3$ at high frequencies). The integrated likelihood $\mathcal{L}(\Delta T_{\rm cmb})$ is shown in Figure 17. The rms obtained by maximizing $\mathcal{L}(\Delta T_{\rm cmb})$ is

$$\delta T_{\rm rms} = 82^{+12.1}_{-9.1}\ \mu{\rm K}, \tag{37}$$

where quoted errors define the 68% highest probability density (HPD) confidence interval.

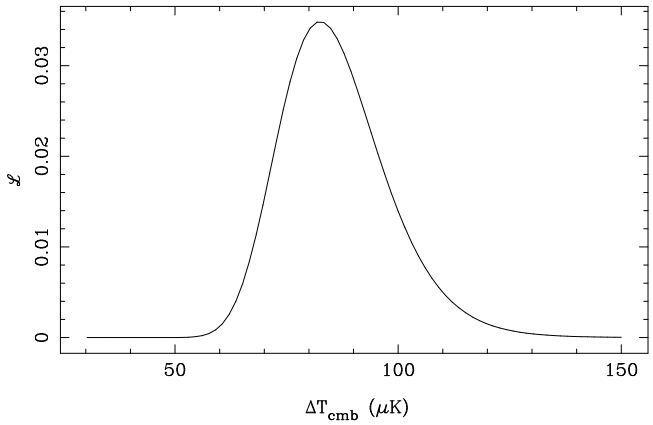

FIG. 17.— Integrated likelihood function $\mathcal{L}(\Delta T_{\rm cmb})$ for the CMBR component.

13. WINDOW FUNCTIONS

The theoretical sky temperatures can be expanded in spherical harmonics $T(\mathbf{x}_i) = \sum_{l,m} a_l^m Y_l^m(\mathbf{x}_i)$, so that assuming rotational symmetry, the expected value of the 2-pt correlation for fields i and j separated by an angle χ_{ij} on the sky is given by

$$\langle T_i \cdot T_j \rangle = \frac{1}{4\pi} \sum_l (2l+1) C_l P_l(\cos\chi_{ij}), \tag{38}$$

where P_l are the associated Legendre polynomials, and $C_l = \langle |a_l^m|^2 \rangle$ are the elements of the theoretical angular power spectrum (Peebles 1992). What we measure are the theoretical sky temperatures convolved with the telescope beam and switching strategy, i.e., $\Delta T_i = T_i * B_i$ (for the RING5M experiment, $B_i(\theta,\phi)$ is given by the function in Figure 1), so that defining $C_{ij\,B} \equiv B_i \otimes B_j$, where $\otimes$ denotes cross-correlation, and letting $*$ denote convolution, Eq. 38 gives

$$C_{ij\,{\rm cmb}} = \frac{1}{4\pi} \sum_l (2l+1) C_l P_l(\cos\chi_{ij}) * C_{ij\,B}$$

$$\equiv \frac{1}{4\pi} \sum_l (2l+1) C_l W_l^{ij} \tag{39}$$

for the theoretical elements of the covariance matrix in Eq. 35. In CMBR parlance, the function $W_l^{ij} \equiv P_l(\cos\chi_{ij}) * C_{ij\,B}$ is known as a *window function*. For the RING5M experiment, a good approximation to the zero-lag ($\chi_{ii} \equiv 0$) window function is given by $W_l^{ii} = W_l^{bm} \cdot W_l^{sw}$, where $W_l^{bm} = \exp[-l(l+1)\sigma^2]$ (Silk & Wilson 1980, Bond & Efstathiou 1984), with $\sigma = 3'.13$, and $W_l^{sw} = \frac{3}{2} - 2P_l(\cos\chi_s) + \frac{1}{2}P_l(\cos 2\chi_s)$, with $\chi_s = 22'.16$.

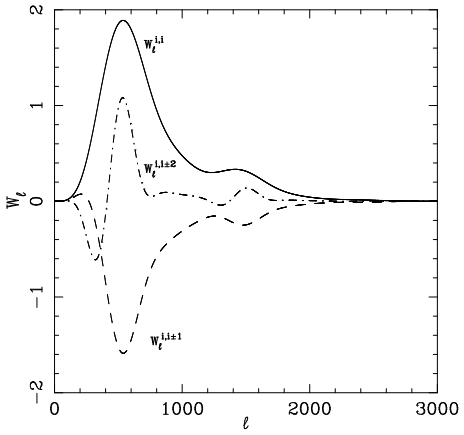

FIG. 18.— Comparison of $0'$ ($W_l^{i,i}$), $22'$ ($W_l^{i,i+1}$) and $44'$ lag ($W_l^{i,i+2}$) window functions for the RING5M experiment, characterizing correlations between neighboring fields.

14. DATA CORRELATIONS

14.1. *Point Sources*

In general, point sources are not measured coincidentally with the Ring data, but are instead assumed to have constant flux densities and associated errors over timescales of a month (the typical time between VLA flux monitoring sessions during 1996) or longer. Since any source affects at least three fields through the double switching, subtraction of source contributions introduces correlated noise between neighboring fields, contributing

$$\sigma_{ij}^2 = \sum_k \langle b_{ik} \rangle \langle b_{jk} \rangle \sigma_k^2 \tag{40}$$

to the covariance matrix, where the b_{ik} are the beam weighting factors for the k^{th} source in the i^{th} field, and σ_k is the error associated with the flux density of the k^{th} source. Although these covariances are included in the likelihood analysis, the effect is negligible, even for the 1994-1995 RING5M data, for which source errors are enlarged to include variability.

14.2. *Noise Correlations*

An analysis of the long-term noise characteristics of the Ring5m data indicates the presence at 31.7 GHz of correlated noise between fields separated by $22'$. The amplitude of this correlated noise is approximately $40\,\mu$K, or $3-4$% of the uncorrelated noise in a single scan on a Ring field (see

§7.3). Analysis of subsets of the 31.7 GHz data suggest no obvious source for this component; we note however that its amplitude is of the same order as the observed season-to-season fluctuations in the 31.7 GHz mean levels (see §7.4), suggesting that the same component may be responsible for both.

While the origin of this correlated noise is not well understood, independent confirmation of its presence can be seen through its effect on the data correlations; the mean Ring5m data set shows only half of the anti-correlation for nearest-neighbor fields expected for a 3-beam chopped experiment, $C_{i,i\pm1}/C_{ii} = -2/3$.

Our approach is to include the noise correlation as a free parameter in our model for the covariance matrix, i.e., we let

$$\sigma_{ij}^2 = \delta_{ij}\sigma_{ii}^2 + \delta_{i\pm1,j}\sigma_{\rm n}^2 \tag{41}$$

in Eq. 35, where $\sigma_{\rm n}$ is the amplitude of the correlated noise, and σ_{ii}^2 are the variances in the field means, as before. As with the foreground spectral index, we integrate out the dependence on the noise correlation amplitude to obtain an estimate of the CMBR variance. Thus, the full form of the likelihood function $\mathcal{L}(\Delta T_{\rm cmb})$ in Eq. 36 is

$$\mathcal{L}(\Delta T_{\rm cmb}) = \iint \mathcal{L}(\Delta T_{\rm cmb}, \beta, \sigma_{\rm n}) d\beta\, d\sigma_{\rm n}. \tag{42}$$

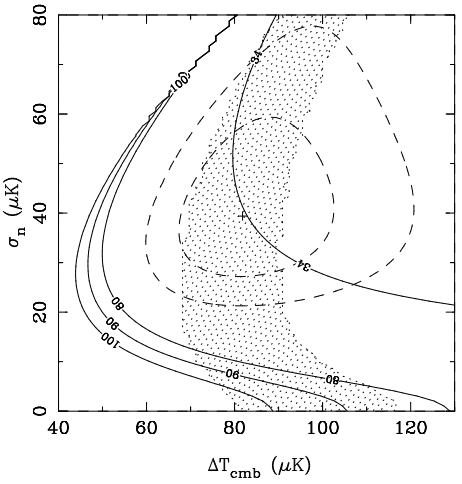

FIG. 19.— Integrated likelihood $\mathcal{L}(\Delta T_{\rm cmb}, \sigma_n)$ for the CMBR component extracted at the maximum likelihood value of β. Contours are $\chi^2 \equiv \mathbf{t}^T\mathbf{C}^{-1}\mathbf{t}$ for the 36 Ring5m fields (see §12). Dashed contours are the 68% and 95% $\Delta T_{\rm cmb} - \sigma_{\rm n}$ confidence regions. Stippled region is the locus of 1-D 68% confidence intervals in $\Delta T_{\rm cmb}$ at each value of $\sigma_{\rm n}$.

In Figure 19, we plot $\mathcal{L}(\Delta T_{\rm cmb}, \sigma_{\rm n})$ for the CMBR component extracted at the maximum likelihood value of the foreground spectral index ($\beta \simeq -2.7$), along with contours of constant χ^2, where $\chi^2 = \mathbf{t}^T\mathbf{C}^{-1}\mathbf{t}$ (c.f. Eq. 34). The peak of the likelihood function occurs for $\sigma_{\rm n} = 41^{+20.5}_{-11.8}$ μK. Also shown is the locus of 68% confidence intervals on $\Delta T_{\rm cmb}$ which would be obtained if the correlated noise component were held fixed at the corresponding value on the y-axis. As can be seen from the figure, maximum likelihood models which neglect these correlations are grossly discrepant with the data ($\chi^2 \gg 34$).

15. BAND POWER

The mass fluctuation power spectrum is often taken to be scale-invariant at small wave number, $\mathcal{P}(k) \propto k$ (i.e., the Harrison-Zel'dovich spectrum), leading to a CMBR angular power spectrum with $C_l^{-1} \propto l(l+1)$ on large angular scales (Peebles 1992). As a result, the *band power* (Bond 1995)

$$\delta T_l \equiv \sqrt{l(l+1)C_l/2\pi} \tag{43}$$

is expected to be flat at small l, and is most often the quantity predicted by theory.

With the experimental rms obtained from the diagonal elements of the covariance matrix in Eq. 39, $\delta T_{\rm rms} \equiv \sqrt{C_{ii\,\rm cmb}}$, it can be seen that the band power is related to the rms by

$$\delta T_{\rm rms} = \sqrt{\sum_l \frac{(l+\frac{1}{2})}{l(l+1)} \delta T_l^2 W_l^{ii}}, \tag{44}$$

so that defining

$$I(W_l^{ii}) = \sum_l \frac{(l+\frac{1}{2})}{l(l+1)} W_l^{ii}, \tag{45}$$

the weighted mean of the band power over the window function is given by

$$\delta T_{l_e} = \delta T_{\rm rms}/\sqrt{I(W_l^{ii})}. \tag{46}$$

The integral of the window function is $I(W_l^{ii}) = 1.96$, yielding

$$\delta T_{l_e} = 59^{+8.6}_{-6.5}\ \mu{\rm K},\ l_e = 589^{+167}_{-228}, \tag{47}$$

where $l_e = I(lW_l^{ii})/I(W_l^{ii})$ and errors on l_e are the points at which the window function falls by $e^{-0.5}$. Errors on the band power are the 68% HPD confidence interval, and reflect sample variance, measurement error and 4.3% calibration error.

16. DISCUSSION

The goal of the RING5M experiment was to determine the CMBR anisotropy on $7' - 22'$ scales, corresponding to $\sim$ 10 Mpc at decoupling. We detect structure independently at 14.5 and 31.7 GHz well above the noise limits of the data. Observation of northern fields near transit ensures that the local environment is nearly identical from one field to the next; although the 14.5 GHz data show a parallactic angle dependence indicative of contamination by RFI, observations of the fields at both upper and lower culmination confirm that RFI contributes the same offset to each field and thus does not affect our estimate of the variance. Numerous internal consistency checks (§7-9) demonstrate that the structure observed in the RING5M is reproducible from year to year at both frequencies, while the strong correlation between frequencies confirms that the structure originates on the sky (§11). Careful characterization of both telescopes (§6) and an extensive program of observations of calibrator sources (§5) reduce our total calibration error to 4.3% — well below the sample variance of the experiment.

With discrimination of foregrounds provided by our low frequency channel and accurate removal of point source

contamination using the VLA, we can state with confidence that 76% of the raw variance, or 88% of the source-subtracted variance at 31.7 GHz is due to the CMBR (see Table 7). (A breakdown of the 31.7 GHz data set into CMBR, point source and foreground contributions is given in Table 8.)

Our 14.5 GHz observations of the NCP have also resulted in the detection of an anomalous component of Galactic emission. The detection of this component is a cautionary tale for future CMBR experiments; whether the emission is due to high-temperature free-free emission correlated with Galactic dust (Leitch et al. 1997), or to some novel type of emission from the dust itself (Ferrara & Dettmar 1994, Draine & Lazarian 1998), our results suggest that emission associated with Galactic IR cirrus is potentially a serious contaminant of small-scale anisotropy experiments even below 100 GHz.

17. CONCLUSION

A likelihood analysis of the RING5M data yields, for the CMBR component alone, a temperature rms of $\delta T_{\rm rms} = 82^{+12.1}_{-9.1}$ μK, or equivalently, a band power of $\delta T_l \equiv \sqrt{l(l+1)C_l/2\pi} = 59^{+8.6}_{-6.5}$ μK (68% HPD confidence interval) at $l_e = 589^{+167}_{-228}$.

On $2'$ scales, the OVRO NCP 95% confidence upper limit of $\Delta T/T < 1.7 \times 10^{-5}$ has recently been confirmed by the SuZIE experiment, which set an upper limit of $\Delta T/T < 2.1 \times 10^{-5}$ at nearly the same angular scale (Church et al. 1997). While these results cannot strongly differentiate between varieties of closed universes, as anisotropies are exponentially damped at arcminute scales for all of these models (Silk & Wilson 1980), the RING5M, NCP and SuZIE results together constitute a significant constraint on open universe models; models with $h = 0.3 - 0.7$ and $\Omega_b = \Omega_0 = 0.2$ over-predict small-scale power by $35\% - 50\%$ at $l_{\rm RING5M}$, and by $10\% - 35\%$ over the NCP upper limit at $l_{\rm NCP}$. Open models with baryon density close to the lower bound allowed by big bang nucleosynthesis calculations, $\Omega_b h^2 \sim 0.015$ (Wagoner 1973, Dicus 1982), can reproduce the band powers observed at arcminute scales but severely under-predict the power observed by degree-scale experiments.

Taken together, the RING5M and NCP results indicate a decrease in the angular power spectrum between $l \sim 600$ and $l \sim 2000$. If the collection of data near l of a few hundred can be taken as evidence for a rise in the power spectrum toward small scales, then the RING5M band power is consistent with a peak in the power spectrum near $l \sim 200$. A χ^2 fit to the data in Figure 19 for a range of model power spectra shows that the data are consistent with $\Omega_0 = 1$ in a Λ-model with $\Omega_b h^2 = 0.015$ and $\Omega_\Lambda = 0.7$ or a standard CDM scenario with $\Omega_b h^2 = 0.0045$, shown in Figure 19. Although increasing Ω_b dramatically affects the amplitude of the first acoustic peak, the competing effects of damping at small scales and enhancement of compressional peaks with increasing Ω_b means that the RING5M result cannot strongly constrain Ω_b in a flat universe.

Recent observations with the Cambridge Anisotropy Telescope (CAT) have resulted in a detection of anisotropy on angular scales directly comparable to those probed by the RING5M experiment (Scott et al. 1996). The broad-band power reported in this paper is in good agreement with the CAT detection of $\delta T_{l_e}/T = 1.8^{+0.7}_{-0.5} \times 10^{-5}$ at $l = 590$. Given the result reported here, and the NCP and SuZIE results at higher l, there can be little doubt that the CMBR spectrum drops significantly between $l \sim 600$ and $l \sim 2000$, as expected in flat cosmological models.

We are indebted to Harry Hardebeck, Mark Hodges and Russ Keeney for their consistently exceptional work on the 5.5-meter and 40-meter telescopes and receivers. We thank Marion Pospiezalski at NRAO and Javier Bautista at JPL for providing the HEMT amplifiers upon which this experiment is based. We thank John Carlstrom for the loan of a HEMT amplifier, and Bharat Ratra and Ken Ganga for pointing out an error in the manuscript. We are grateful to U. Seljak and M. Zaldarriaga for placing CMBFAST in the public domain. The work at the California Institute of Technology was supported by NSF grants AST-9119847 and AST-9419279. The VLA is an instrument of the National Radio Astronomy Observatory, a facility of the National Science Foundation operated under cooperative agreement by Associated Universities, Inc.

TABLE 8
SUMMARY OF CONTRIBUTIONS TO THE 31.7 GHZ RING FIELD MEANS[a]

Field	$\overline{\Delta T}_{\rm raw}$ (μK)	$\epsilon_{\rm raw}$ (μK)[b]	$\overline{\Delta T}_{\rm src}$ (μK)	$\epsilon_{\rm src}$ (μK)	$\overline{\Delta T}_{\rm cmb}$ (μK)	$\epsilon_{\rm cmb}$ (μK)	$\overline{\Delta T}_{\rm fore}$ (μK)	$\epsilon_{\rm fore}$ (μK)
OV5M0024	75.88	17.63	143.66	17.07	72.73	50.34	−140.52	20.38
OV5M0104	−118.54	17.73	−146.49	17.28	−52.91	45.35	80.85	19.14
OV5M0144	−43.42	17.11	−9.83	0.84	−20.42	21.49	−13.17	5.43
OV5M0224	110.99	15.77	20.27	1.15	36.65	20.09	54.08	5.36
OV5M0304	−86.21	16.35	−10.60	0.90	−55.68	20.43	−19.93	4.86
OV5M0344	−19.82	17.35	1.72	0.06	−21.33	21.64	−0.22	5.19
OV5M0424	90.33	16.07	10.75	0.28	114.66	20.45	−35.07	5.71
OV5M0504	−13.56	16.32	1.92	0.05	−6.60	20.38	−8.89	4.97
OV5M0544	−11.28	16.50	2.62	0.55	−27.46	20.55	13.56	4.82
OV5M0624	96.01	15.60	0.05	1.87	100.92	19.72	−4.96	4.96
OV5M0704	132.13	15.87	5.30	0.71	174.83	19.84	−48.00	4.77
OV5M0744	12.64	15.29	−1.23	0.65	18.66	19.16	−4.79	4.75
OV5M0824	−122.33	13.87	1.80	0.29	−73.66	17.33	−50.47	4.21
OV5M0904	145.15	14.56	4.62	0.36	99.82	18.16	40.72	4.34
OV5M0944	45.37	15.75	−0.87	0.35	94.81	19.68	−48.58	4.67
OV5M1024	33.42	14.26	13.68	0.71	5.21	19.73	14.53	6.88
OV5M1104	0.56	15.12	8.38	0.69	−67.08	19.19	59.27	4.93
OV5M1144	−78.24	15.07	−21.47	1.17	14.13	20.43	−70.89	6.25
OV5M1224	109.97	14.63	58.15	2.32	−11.15	23.51	62.97	9.28
OV5M1304	−62.25	14.80	−21.74	2.38	−38.47	19.74	−2.03	5.81
OV5M1344	−83.76	14.86	18.59	3.58	−79.56	19.29	−22.80	4.84
OV5M1424	−37.67	15.06	−28.83	3.61	−34.28	19.93	25.45	5.97
OV5M1504	106.89	15.74	48.17	6.14	22.48	22.14	36.24	7.48
OV5M1544	−46.12	16.04	−11.72	2.61	−27.78	20.35	−6.63	5.07
OV5M1624	−68.42	15.85	−0.91	0.29	−71.48	19.84	3.96	4.93
OV5M1704	−48.09	15.69	−9.81	1.45	−33.43	19.70	−4.84	4.85
OV5M1744	35.44	16.18	22.33	1.88	−28.20	20.50	41.31	5.26
OV5M1824	−126.52	15.40	−11.98	1.70	−102.90	19.47	−11.64	5.03
OV5M1904	66.62	16.01	−1.79	0.64	60.59	19.99	7.82	4.80
OV5M1944	−39.11	15.28	9.50	0.53	−32.86	19.22	−15.75	4.94
OV5M2024	−192.57	16.47	−0.89	0.71	−169.52	20.67	−22.15	5.17
OV5M2104	175.60	16.14	−0.97	0.41	157.75	20.30	18.83	5.20
OV5M2144	−13.04	16.62	8.55	1.72	−59.85	22.04	38.26	7.05
OV5M2224	176.05	16.63	12.56	0.71	149.43	21.40	14.07	5.93
OV5M2304	−142.53	17.61	−7.96	0.60	−119.42	21.99	−15.16	5.22
OV5M2344	−59.58	18.60	−105.50	12.23	11.36	35.07	34.57	10.66

[a]Equivalent R-J temperature.

[b]Errors are 1σ rms in the sample mean.

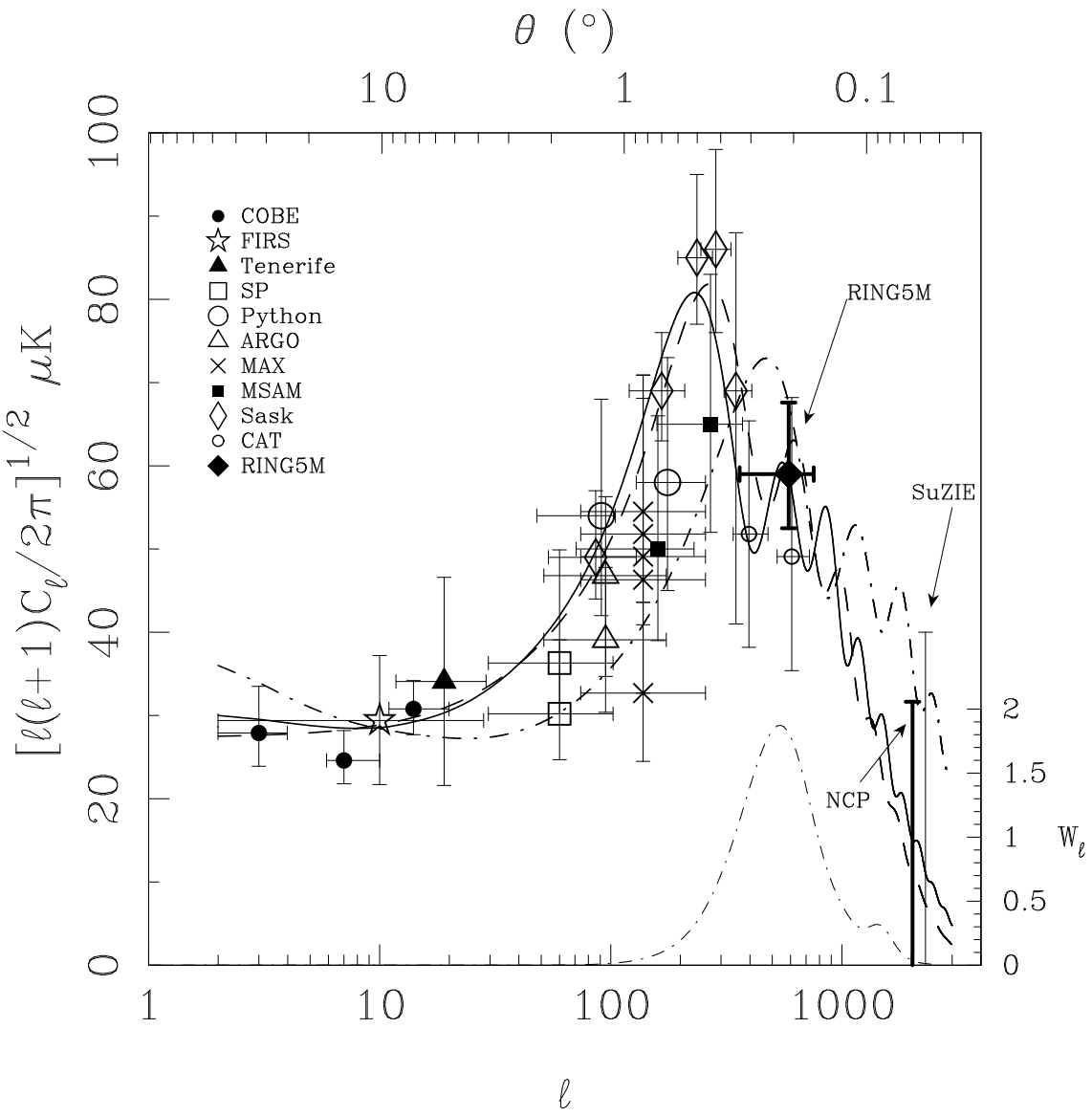

FIG. 20.— CMBR anisotropy measurements, shown with a Λ- model (solid line) with $\Omega_b h^2 = 0.015, \Omega_\Lambda = 0.7$, and $\Omega_0 = 1$, a standard CDM model (dashed line) with $\Omega_b h^2 = 0.0045$, and an open model (dot-dashed line) with $\Omega_b h^2 = 0.015$ and $\Omega_0 = 0.3$. At bottom is the RING5M zero-lag window function (see §13). Indicated in bold are the OVRO RING5M detection of anisotropy at $l_e = 589$ (this paper) and the 95% confidence upper limit from the OVRO NCP experiment (Readhead et al. 1989). Other data points are: COBE (Hinshaw et al. 1996), FIRS (Ganga 1994), Tenerife (Hancock et al. 1997), SP (Gundersen et al. 1995), Python (Platt et al. 1997), ARGO (de Bernardis et al. 1994), MAX (Tanaka et al. 1996), Saskatoon (Netterfield et al. 1997), CAT (Scott et al. 1996) and SuZIE (Church et al. 1997). Models were computed using CMBFAST (Seljak & Zaldarriaga 1996, Seljak & Zaldarriaga 1997, Zaldarriaga et al. 1998).

REFERENCES

Baars, J. W. M., Genzel, R., Pauliny-Toth, I. I. K. & Witzel, A. 1977, Astron. Astrophys., 61, 99.
Banday, A. J. & Wolfendale, A. W. 1991, MNRAS, 248, 705.
Bond, J. R. 1996, in Cosmology and Large Scale Structure, Les Houches Session LX, August 1993, ed. R Schaeffer (Amsterdam: Elsevier), 469.
Bond, J. R. 1995, Astrophys. Lett., 32, 63.
Bond, J. R. & Efstathiou, G. 1984, ApJ, 285, 45.
Cheng, E. S., Cottingham, D. A. & Fixsen, D. J. 1997, ApJ, 488, 59.
Church, S. E., Ganga, K. M. et al. 1997, ApJ, 484, 523-537.
de Bernardis, P., Aquilini, E., Boscaleri, A., Depetris, M., Dandreta, G., Gervasi, M., Kreysa, E., Martinis, L. et al. 1994, ApJ, 422, 33.
Dent, W. A. 1972, ApJ, 177, 93.
Dicus, D. A., Kolb, E. W., Gleeson, A. M., Sudarshan, E. C. G., Teplitz, V. L. & Turner, M. S. 1982, Phys. Rev. D, 26, 2694.
Draine, B. & Lazarian, A. 1998, ApJ, 494, 19.
Ferrara, A., Dettmar, R. J. 1994, ApJ, 427, 155.
Ganga, K., Page, L., Cheng, E. S., Meyer, S. 1994, ApJ, 432, 15.
Gary, B. 1974, Astron. J., 79, 318.
Gundersen, J. O., Lim, M., Staren, J., Wuensche, C. A., Figueiredo, N., Gaier, T. C., Koch, T., Meinhold, P. R., et al. 1995, ApJ, 443, 57.
Hancock, S., Rocha, G., Lasenby, A. N., & Gutierrez, C. M. 1998, MNRAS, 294, L1.
Hancock, S., Gutierrez, C. M., Davies, R. D., Lasenby, A. N., Rocha, G. Rebolo, R., Watson, R. A., & Tegmark, M. 1997, MNRAS, 289, 505.
Hinshaw, G., Banday, A. J., Bennett, C. L., Gorski, K. M., Kogut, A., Smoot, G. F., & Wright, E. L., 1996, ApJ, 464, 17.
Kogut, A., Banday, A. J., Bennett, C. L., Gorski, K. M., Hinshaw, G., & Reach, W. T. 1996, ApJ, 460, 1.
Kolb, E. W., & Turner, M. S. 1990, The Early Universe (Redwood City: Addison-Wesley).
Leitch, E. M. 1998, PhD thesis, Caltech.
Leitch, E. M., Myers, S. T., Readhead, A. C. S. & Pearson, T. J. 1997, ApJ, 486, 23.
Myers, S. T., Readhead, A. C. S. & Lawrence, C. R. 1993, ApJ, 405, 8.

Myers, S. T., Baker, J. E., Readhead, A. C. S., Leitch, E. M. & Herbig, T. 1997, ApJ, 485, 1.
Netterfield, C. B. 1995, PhD thesis, Princeton.
Netterfield, C. B, Devlin, M. J., Jarosik, N., Page, L. & Wollack, E. 1997, A.J., 474, 47.
Peebles, P. J. E. 1992, Principles of Physical Cosmology (Princeton: Princeton Univ. Press).
Platt, S. R., Kovac, J., Dragovan, M., Peterson, J. B. & Ruhl, J. E. 1997, ApJ, 475, 1.
Reach, W. T., Dwek, E., Fixsen, D. J., Hewagama, T., Mather, J. C., Shafer, R. A., Banday, A. J., Bennett, C. L., et al. 1995, ApJ, 451, 188.
Readhead, A. C. S., Lawrence, C. R., Myers, S. T., Sargent, W. L. W., Hardebeck, H. E. & Moffet, A. T. 1989, ApJ, 346, 566.
Reich, P. & Reich, W. 1988, A&A Suppl., 74, 7.
Rengelink, R. B., Tang, Y., Debruyn, A. G., Miley, G. K., Bremer, M. N., Rottgering, H. J. A., Bremer, M. A. R. 1997, A&A Suppl., 124, 259.
Scott, P. F., Saunders, R., Pooley, G., Osullivan, C., Lasenby, A. N., Jones, M., Hobson, M. P., Duffettsmith, P. J. 1996, ApJ, 461, 1.
Seljak, U. & Zaldarriaga, M. 1997, CMBFAST (available on the World-Wide-Web at `http://arcturus.mit.edu:80/~matiasz/CMBFAST/cmbfast.html`).
Seljak, U. & Zaldarriaga, M. 1996, ApJ, 469, 437.
Silk, J. & Wilson, M. L. 1980, Phys. Scripta, 21, 708.
Sivia, D. S. 1996, Data Analysis: A Bayesian Tutorial (Oxford: Clarendon Press).
Smoot, G. F., Bennett, C. L., Kogut, A., Wright, E. L., Aymon, J., Boggess, N. W., Cheng, E. S., Deamici, G., et al. 1992, ApJ, 396, 1.
Tanaka, S. et al. 1996, ApJ, 468, 81.
Wagoner, R. V. 1973, ApJ, 179, 343.
Wright E. L., Mather J. C. & Bennett, C. L. 1991, ApJ, 381, 200.
Zaldarriaga, M., Seljak, U. & Bertschinger, E. 1998, ApJ, 494, 491.